A monthly 0.05° terrestrial evapotranspiration product (1982-2018) for the Tibetan Plateau

Ling Yuan [1,2], Xuelong Chen[1,4,6]*, Yaoming Ma[1,2,3,4,5,6]*, Cunbo Han[1,4,6], Binbin Wang[1,4,5,6], Weiqiang Ma[1,4,6]

[1] Land-Atmosphere Interaction and its Climatic Effects Group, State Key Laboratory of Tibetan Plateau Earth System, Resources and Environment (TPESRE), Institute of Tibetan Plateau Research, Chinese Academy of Sciences, Beijing 100101, China.

[2] College of Earth and Planetary Sciences, University of Chinese Academy of Sciences, Beijing 100049, China

[3] College of Atmospheric Science, Lanzhou University, Lanzhou 730000, China

[4] National Observation and Research Station for Qomolongma Special Atmospheric Processes and Environmental Changes, Dingri 858200, China

[5] Kathmandu Center of Research and Education, Chinese Academy of Sciences, Beijing 100101, China

[6] China-Pakistan Joint Research Center on Earth Sciences, Chinese Academy of Sciences, Islamabad 45320, Pakistan

Corresponding author and address:

Xuelong Chen, Dr., Prof., x.chen@itpcas.ac.cn

Yaoming Ma, Dr., Prof., ymma@itpcas.ac.cn

Building 3, No.16 Lincui Road, Chaoyang District, Beijing 100101, China

Abstract

Evapotranspiration (ET) is an important component of the water balance system in the "Asian water tower" region, the Tibetan Plateau (TP). However, accurately monitoring and understanding the spatial and temporal variability of the ET components (soil evaporation E_s, canopy transpiration E_c, and intercepted water evaporation E_w) on the TP remains gravely challenging due to the paucity of observational data for this remote area. In this study, the 37 years (1982–2018) of monthly ET component data for the TP were produced using the MOD16-STM (MOD16 soil texture model), which uses the recently available soil properties, meteorological conditions, and remote sensing datasets. The estimated ET results correlate well with the measurements from nine flux towers, with a low root mean square error of 13.48 mm/month, mean bias of 2.85 mm/month, coefficient of determination of 0.83, and index of agreement of 0.92. The annual averaged ET for the entire TP (specified as elevations higher than 2500 m) is about 0.93 ± 0.037 Gt/year. The main contribution of the ET on the TP comes from the soil, with the E_s accounting for 84% of the ET. The results of this study indicate that the ET in most of the central and eastern parts of TP showed a significant upward trend with a rate of about 1-4 mm/year ($P<0.05$) during the period from 1982 to 2018. The averaged ET increasing trend for the whole TP over the past 37 years was around 0.96 mm/year. The increase trend during the 37 years can be explained by the warming and wetting climate on the TP. The MOD16-STM ET data exhibited an acceptable performance over the TP compared with previous results. MOD16-STM ET can accurately estimate actual ET for research in water resource management, drought monitoring and ecological change. The whole datasets are freely available at the Science Data Bank (http://doi.org/10.11922/sciencedb.00020, Y. Ma*, X.Chen*, L. Yuan, 2021) and the National Tibetan Plateau Data Center (TPDC) (https://data.tpdc.ac.cn/en/disallow/e253621a-6334-4ad1-b2b9-e1ce2aa9688f/, http://doi.org/10.11888/Terre.tpdc.271913, L. Yuan, X.Chen*, Y. Ma*, 2021).

Keywords: Evapotranspiration; MOD16-STM; Climate change; Asian water tower; Tibetan Plateau

1. Introduction

The Tibetan Plateau (TP) (24–40°N, 70–105°E) is known as the Asian water tower (Immerzeel et al., 2010, 2020; Yao et al., 2012; Xu et al., 2019) due to its unique geographical and ecological characteristics. Evapotranspiration (ET) is a very important component of the water balance of the Asian water tower. The land cover on the TP is predominantly grassland (a coverage > 47%) and sparse vegetation or bare soil (coverage > 33%) based on the Moderate Resolution Imaging Spectroradiometer (MODIS) landcover (MCD12C1) dataset (Fig. 1). Most of the TP is arid or semi-arid area. The TP is experiencing accelerated changes in its hydrological cycle due to global warming (Yang et al., 2014; Kuang et al., 2016; Zohaib et al., 2017). Meanwhile, accurate monitoring of the spatial and temporal variability of the ET remains challenging due to the complex environment of the TP. In addition, how the ET over the TP will change under the background of global warming is critical for analyzing the impacts of changes in the water balance of the Asian water tower on the local people's lives.

In the last few years, a wide variety of ET datasets have been compiled to improve estimations of the ET on the TP, i.e., the complementary relationship (CR) model (Ma et al., 2019; Wang et al., 2020), the surface energy balance system (SEBS) model (Chen et al., 2014, 2021; Zhong et al., 2019; Han et al., 2017, 2021), and the Penman–Monteith model with remote sensing (RS-PM) (Wang et al., 2018; Song et al., 2017; Chang et al., 2019; Ma et al., 2022) etc.. A considerable variance among the ET products for the TP still exhibit (Peng et al., 2016; Baik et al., 2018; Li et al., 2018; Khan et al., 2018). The eddy-covariance measurement (Shi et al., 2014; You et al., 2017; Yang et al., 2019; Ma et al., 2020) have used to study the ET on the TP. Furthermore, the reanalysis datasets have also used to investigate the ET on the TP (Shi et al., 2014; Dan et al., 2017; Yang et al., 2019; De Kok et al., 2020). A ET dataset of 18 years (2001–2018) was produced by Han et al., 2021. Previous studies have obtained accurate ET estimates after improving the canopy conduction algorithm in the Penman–Monteith model (Leuning et al., 2008; Zhang et al., 2010; Li et al., 2015; Zhang et al., 2016, 2019; Gan et al., 2018). The Penman–Monteith algorithm has also been used to separately estimate the canopy transpiration (E_c), soil evaporation (E_s), and intercepted water evaporation (E_w) (Mu et al., 2011; Zhang et al., 2010) for global land. These ET products perform poorly in TP areas with sparse vegetation or arid to semi-arid climates, as well as in areas with inadequate water supplies (Zhang et al., 2010; Li et al., 2014b; Song et al., 2017; Baik et al., 2018; Li et al., 2018; Khan et al., 2018). The poor performance of the MOD16 Penman–Monteith model (Mu et al. 2011) in the arid to semi-arid areas of the TP is due to the fact that the algorithm does not take into account the dominant role of the topsoil information (topsoil texture and topsoil moisture (SM)) in controlling the evaporation processes (Yuan et al., 2021). Scientists still have difficulties to accurately separate and validate

the ET components on the TP, even though the total ET estimates are consistent across different products (Lawrence et al., 2007; Blyth and Harding, 2011; Miralles et al., 2016). TP land covers is dominated by the short and sparse vegetation. Soil moisture may play an important role on the ET estimates for the TP region. The Penman–Monteith algorithm has been used to test the performance of the ET estimation on the TP (Wang et al., 2018; Ma et al., 2022). However, the effects of the SM on the evaporation resistance and stomatal conductance are not included in these studies. The enhanced Penman–Monteith model, MOD16-STM (MOD16 soil texture model), redefines the E_s and E_c module to take into account the impacts of SM on soil evaporation resistance, with the help of eddy-covariance observations on the TP (Yuan et al., 2021). Hereby, MOD16-STM may provide us with a high chance to accurately estimate ET`s components.

E_s may account for the vast majority of ET in sparsely vegetated areas, especially in arid and semi-arid areas where bare soil areas are relatively large (Wilcox et al., 2003; Kool et al.,2014; Wang et al., 2018; Ma et al., 2015; Ma and Zhang, 2022). Previous studies have pointed out that 20% to 40% of the global ET comes from Es (Lawrence et al., 2007; Schlesinger and Jasechko, 2014; Wei et al., 2017), which is a fast process influenced by shallow surface water (Koster and Suarez, 1996) and mainly controlled by soil vapor diffusion (Good et al., 2015; Yuan et al., 2022). Therefore, accurate quantification and separation of the E_s could help to improve our understanding of the water and energy cycles on the TP. Nevertheless, quantifying the ET and its components remains a difficult task, since ET process is controlled by the atmospheric demand, soil moisture conditions, and complex interactions between inhomogeneous vegetation and soil properties (Merlin et al., 2016; Wu et al., 2017; Philips et al., 2017; Lehmann et al., 2018). MOD16-STM has the possibility to produce a remote sensing ET and ET component dataset for the satellite age since 1980. Hereby, in this study, the MOD16-STM model, with its drawbacks fully in mind, was used to estimate a long-term ET and ET components dataset (Yuan et al., 2021).

A direct estimation of ET based on topsoil moisture, which is more capable of influencing TP surface water heat exchange, is a more preferable approach. Hence, based on the advantage of the MOD16-STM model for estimating ET on the TP, the goals of this study were (1) to develop a 37-year (1982–2018) 0.05×0.05 monthly ET dataset for the TP; and (2) to quantify the spatial distributions and spatiotemporal variability of the ET and its components over the TP.

2. Materials and methods

2.1 Study area

The Tibetan Plateau (25-40°N, 74-104°E) is about 2.5 million km^2 of land above 2,500 meters in altitudes)

(Fig. 1a). Based on FAO drought index dataset, it is the largest landform unit in Eurasia and mainly includes hyper-arid, arid, semi-arid, and sub-humid climate zones (Fig. 1b). The land cover types are mainly divided into mixed forest, grassland, bare soil, glaciers and snow covered area (Fig. 1c). The topsoil is mainly covered with sandy loam, loam, and clay (Fig.1d). The annual average temperature is about −3.1°C to 4.4°C. The average annual precipitation gradually increases from less than 50 mm in the northwest to more than 1000 mm in the southeast, and most of the precipitation is concentrated in the summer (Ding et al., 2017). The TP has experienced a significant changes in its environment, including: increased precipitation; decreased wind speed, snow days, and radiation; and the thawing of permafrost; melting of glaciers; and greening of vegetation (Kang et al., 2010; Yao et al., 2012; Yang et al., 2014; Kuang et al., 2016; Bibi et al., 2018; Chen et al. 2019).
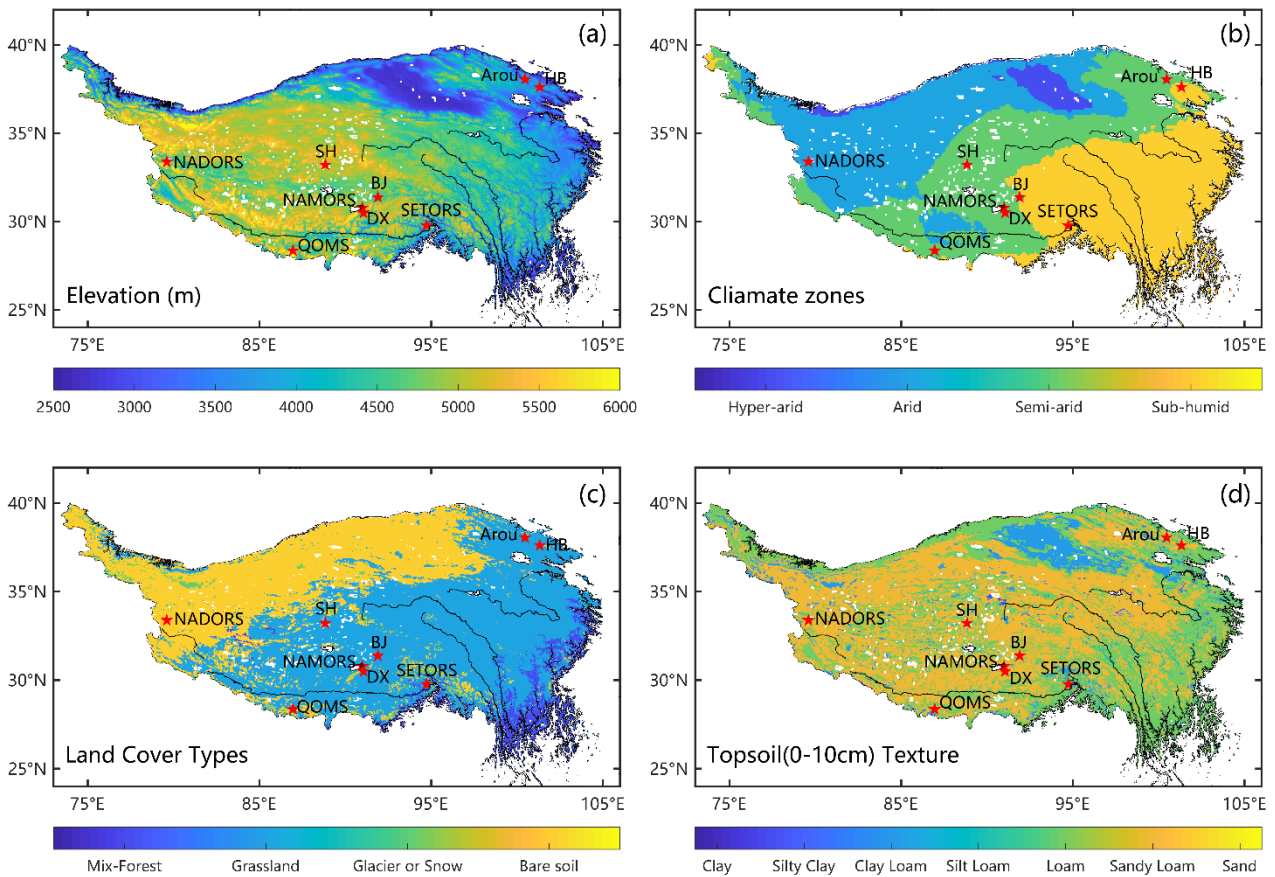
Figure 1. Maps of the (a) topography (STRM), (b) climate zones (FAO aridity index), (c) land cover types (MCD12C1), and (d) soil textures (HWSD) in the study area. The red dots indicate the flux site locations.

2.2 Generation of a long-term series of monthly ET products

In this study, a new dataset of long-term series of monthly ET is produced by the MOD16-STM model. The workflow for calculating the monthly ET using the MOD16-STM model and driving datasets is presented in Fig. 2.
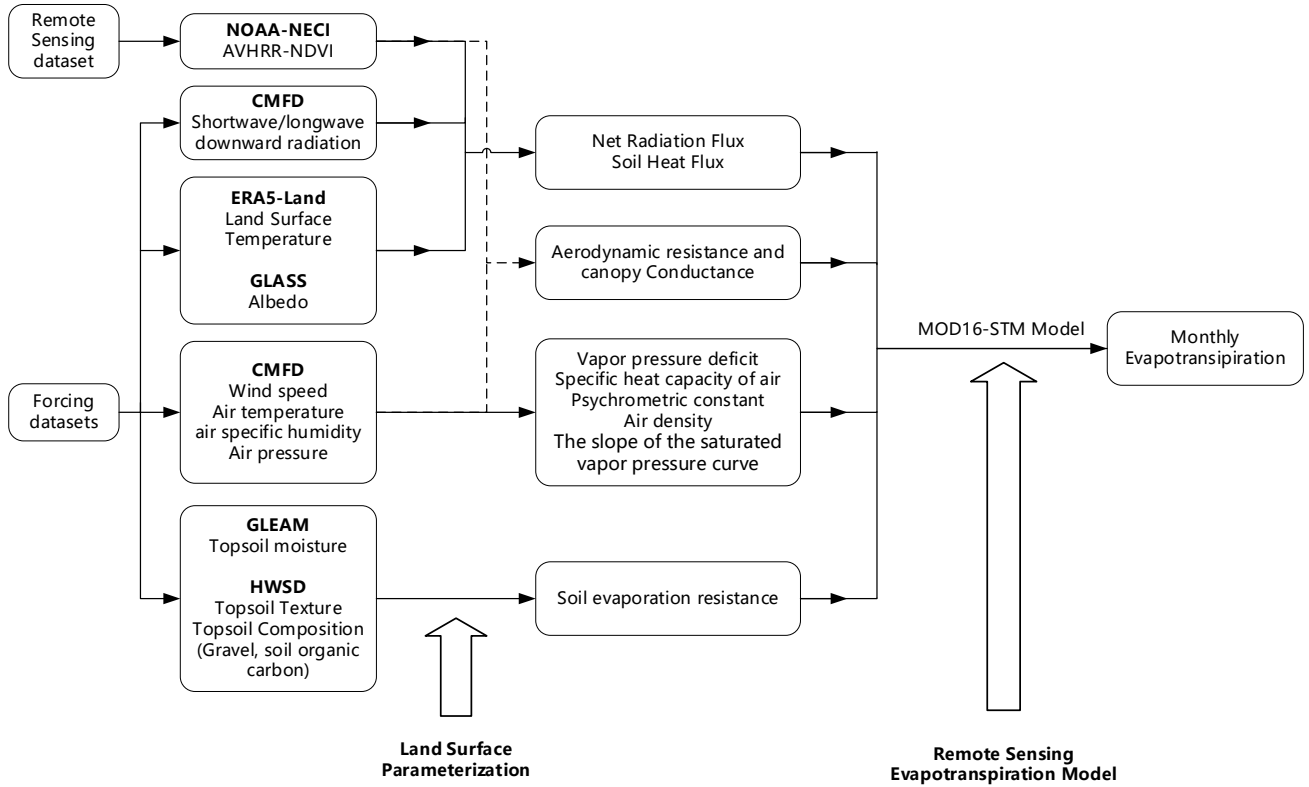
Figure 2. Workflow of the MOD16-STM evapotranspiration product.

2.2.1 Description of MOD16-STM ET model

140   The MOD16-STM model calculates the ET components based on the Penman–Monteith equation as follows:

$$E_c = \frac{(\Delta \times f_c \times (R_n - G_0) + \rho_a \times C_p \times \frac{VPD}{r_a} \times f_c) \times (1 - F_{wet})}{\lambda \times \left(\Delta + \gamma \times (1 + \frac{r_c}{r_a})\right)} \tag{1}$$

$$E_s = \frac{(\Delta \times (1 - f_c) \times (R_n - G_0) + \rho_a \times C_p \times \frac{VPD}{r_a}) \times (1 - F_{wet})}{\lambda \times \left(\Delta + \gamma \times (1 + \frac{r_s}{r_a})\right)} \times \left(\frac{RH}{100}\right)^{\frac{VPD}{\beta}} \tag{2}$$

$$E_w = E_{wet\_s} + E_{wet\_c} \tag{3}$$

The ET is the sum of the three components E_c, E_s, and E_w. E_{wet_s} and E_{wet_c} are the evaporation from the wet soil and wet canopy. More details on how to calculate these two parts can be found in Yuan et al. 2021. Rn is the net radiation flux (W/m^2); G$_0$ is the soil heat flux (W/m^2); ρ_a is the density of the air (kg/m^3); Cp is the specific heat capacity of the air (J/kg/K); VPD is the vapor pressure deficit (hPa); and Δ

is the slope of the saturated vapor pressure curve (hPa/K). γ is the psychrometric constant (hPa/K), and $\gamma = Cp \cdot P_a \cdot M_a / (\lambda \cdot M_w)$, where λ is the latent heat of vaporization(J/kg), and M_a and M_w are the molecular masses of dry air and wet air, respectively. r_a is the aerodynamic resistance (s/m); and r_s is the surface (or canopy) resistance (s/m). Vegetation cover fraction (f_c) is estimated from the NDVI; and F_{wet} is the relative surface wetness.

$$f_c = \left(\frac{NDVI - NDVI_{min}}{NDVI_{max} + NDVI_{min}} \right)^2 \tag{4}$$

R_n and G_0 are calculated as follows:

$$R_n = (1-\alpha) \times SWD + LWD - \varepsilon \times \sigma \times LST^4 \tag{5}$$

$$G_0 = R_n \times (I_c + (1-f_c) \times (I_s - I_c)) \tag{6}$$

where σ is the Stefan-Boltzmann constant (5.67×10^{-8} W/m^2/K^4). I_c (=0.05) and I_s (=0.315) are the ratios of ground heat flux and net radiation for surfaces with the full vegetation cover (Su et al., 2002) and bare soil (differentiated by NDVI < 0.25 in this study) (Yuan et al., 2021), respectively. When $T_a < 5°C$, photosynthesis and transpiration are not active, so E_c is not taken into account. When the LST or $T_a < 0°C$, the sublimation equation is obtained by rewriting the surface energy balance equation using the Clausius–Clapeyron equation for (liquid and frozen) water-vapor equilibrium.

Furthermore, the evaporation of water surface was not estimated in this study because previous studies have specifically studied the evaporation from the lakes on the TP in detail (Wang et al., 2020).

Many previous studies have used the optimized conductance to estimate Ec (Jarvis et al., 1976; Irmak and Mutiibwa, 2010; Zhang et al., 2010; Leuning et al., 2008; Li et al., 2013, 2015), and Es (Sun et al., 1982; Camillo and Gurney, 1986; Sellers et al., 1996; Sakaguchi and Zeng, 2009; Ortega-Farias et al., 2010; Tang et al., 2013). In this study, the aerodynamic resistance (r_a) was calculated from the Monin-Obukhov similarity theory (MOST) (Thom, 1975; Liu et al. 2007), the roughness height of the momentum transfer (z_{0m}) was derived from the canopy height (h_c) following Chen et al. (2013), and the roughness heights of the water vapor transfer z_{0h} were derived follows Yang et al. (2008):

$$r_a = \frac{ln\left(\frac{z_h - d_0}{z_{0h}} - \psi_h\right) ln\left(\frac{z_m - d_0}{z_{0m}} - \psi_m\right)}{k^2 u} \tag{7}$$

where k is the von Karman's constant (0.41), z_h and z_m are the measurement heights of the T_a and wind speed,

d_0 is the displacement height. ψ_m and ψ_h are the stability correction functions for the momentum and heat transfer, respectively. These two variables can be calculated using universal functions and the mathematical forms of the correction terms are as follows (Högström, 1996; Paulson, 1970).

For stable conditions:

$$\psi_m = -5.3\frac{(z_m - z_{0m})}{L} \tag{8}$$

$$\psi_h = -8.0\frac{z_h - z_{0h}}{L} \tag{9}$$

For unstable conditions:

$$\psi_m = 2\ln\left(\frac{1+x}{1+x_o}\right) + \ln\left(\frac{1+x^2}{1+x_o^2}\right) - 2\tan^{-1}x + 2\tan^{-1}x_o \tag{10}$$

$$\psi_h = 2\ln\left(\frac{1+y}{1+y_o}\right) \tag{11}$$

For neutral conditions:

$$\psi_m = \psi_h = 0 \tag{12}$$

In Eqs. (8–11), $x = (1 - z_m/L)^{0.25}$, $x_o = (1 - z_{om}/L)^{0.25}$, $y = (1 - 11.6z_h/L)^{0.5}$, and $y_o = (1 - 11.6z_{oh}/L)^{0.5}$. $L = T_a \cdot u*^2/(k \cdot g \cdot T*)$ is the Obukhov length (m), where $g = 9.8$ m/s^2 and $T*$ is the fractional temperature (K). $T* = -(\theta_s - \theta_a)/(\ln(z_h/z_{oh}) - \psi_h)$, where θ_s can be approximated using the LST and $\theta_a = T_a + z_h \cdot g/C_p$ is the potential temperature (K). The parameterization of $u*$ and L has also been successfully applied on the TP (Chen, et al., 2013; Su et al., 2002). z_{oh} is the roughness length of the heat transfer (m). An parameterization scheme for z_{oh} from Yang et al. (2008) has been widely applied in remote sensing land surface fluxes and land surface models (LSMs) over the TP (Biermann et al., 2014; Chen et al., 2013; Ma et al., 2015). This scheme was also applied in this study:

$$z_{0h} = \frac{70v}{u_*}exp(-7.2u_*^{0.5}|T^*|^{0.25}) \tag{13}$$

where v is the fluid kinematic viscosity ($1.328\times10^{-5}\cdot(P_0/P_a)\cdot(T_a/T_0)^{1.754}$), where $P_0 = 1013$ hPa and T0 = 273.15 K. The MOD16-STM model considers the impacts of the soil classification and soil texture on the soil porosity (θ_{sat}), based on which the water saturation degree of surface soil (SM/θ_{sat}) is used to constrain the evaporation resistance (r_s) and Es estimates as follows:

$$r_s = \exp\left(a + b\times\frac{SM}{\theta_{sat}}\right) \tag{14}$$

where *a* and *b* are empirical parameters for different soil textures (Table A2 and Fig. A1). The θ_{sat} estimated considering the soil organic content (SOC) and gravel content can be obtained from the Soc-Vg scheme (Chen et al., 2012; Zhao et al., 2018):

$$\theta_{sat} = (1 - V_{SOC} - V_g) \times \theta_{sat,m} + V_{SOC} \times \theta_{sat,sc} \tag{15}$$

where $\theta_{sat,m}$ is the porosity of the mineral soil ($\theta_{sat,m} = 0.489 - 0.00126\%$ sand) (Cosby et al., 1984), and $\theta_{sat,sc}$ is the porosity of the *SOC* (0.9 m³/m³ in this study) (Farouki, 1981; Letts et al., 2000). V_{soc} and V_g are the volumetric fractions of the *SOC* and gravel, respectively, and they can be calculated as follows:

$$V_{SOC} = \frac{\rho_p \times (1 - \theta_{sat,m}) \times m_{SOC}}{\rho_{SOC} \times (1 - m_{SOC}) + \rho_p \times (1 - \theta_{sat,m}) \times m_{SOC} + (1 - \theta_{sat,m}) \times \frac{\rho_{SOC} \times m_g}{1 - m_g}} \tag{16}$$

$$V_g = \frac{\rho_{SOC} \times (1 - \theta_{sat,m}) \times m_g}{(1 - m_g) \times \left(\rho_{SOC} \times (1 - m_{SOC}) + \rho_p \times (1 - \theta_{sat,m}) \times m_{SOC} + (1 - \theta_{sat,m}) \times \frac{\rho_{SOC} \times m_g}{1 - m_g}\right)} \tag{17}$$

in which the mineral particle density (ρ_p) and the bulk density of the organic matter (ρ_{soc}) were defined as 2700 kg/m³ and 130 kg/m³, respectively, and m_{soc} and m_g are the organic and gravel percentages in each soil layer, respectively.

The performance of the ET model at the site scale is verified with the ET measurements at the flux station (Appendix A).

2.2.2 Input data

The MOD16-STM model uses various remote sensing datasets, reanalysis datasets, and meteorological forcing datasets to estimate the monthly ET across the entire TP. To avoid spatial and temporal gaps in the final product, specific datasets were selected for use in this study (Table 1). The monthly meteorological forcing data from the China Meteorological Forcing Dataset (CMFD), with a 0.1° spatial resolution for 1982–2018 was obtained from the National Tibetan Plateau Data Center (Yang et al., 2010; He et al., 2020), including the wind speed (wind), air temperature (Ta), air specific humidity (q), air pressure (Pa), shortwave downward radiation (SWD), and longwave downward radiation (LWD). CMFD is downloaded from TPDC (https://data.tpdc.ac.cn/). The land surface temperature (LST) and precipitation (Prec) of the ERA5-Land with a 0.1° spatial resolution and monthly temporal resolution were obtained from European Centre for Medium-Range Weather Forecasts (ECWMF). The albedo (α) product with a 0.05° spatial resolution and 8-day temporal resolution was produced from the Global Land Surface Satellite (GLASS) (Liang et al., 2021). A long-term normalized difference vegetation index (NDVI) dataset with a 0.05° spatial resolution and daily temporal resolution were download

from the National Oceanic and Atmospheric Administration's National Centers for Environmental Information (NOAA-NCEI) (https://www.ncei.noaa.gov/products/climate-data-records/normalized-difference vegetation-index) and was used to calculated the canopy height and LAI (Chen et al., 2013). A topsoil moisture (0–10 cm) dataset with a 0.25° spatial resolution and monthly temporal resolution was obtained from the Global Land Evaporation Amsterdam Model (GLEAM) (Miralles et al., 2011). This dataset has been validated to perform well across the TP (Liu et al., 2021). The upward surface longwave radiation (LWU) was derived from the LST using the Stefan-Boltzmann Law. The emissivity (ε) of the mixed pixels were calculated using the specific emissivity of the vegetated (ε_v) and bare (ε_s) land surfaces, following Sobrino et al. (2004). The Harmonized World Soil Database v1.2 (HWSD) provides reliable soil texture and soil property data (Wieder et al., 2014). These data were used to calculate the soil evaporation resistance. The daily and 8-day input data were averaged over the temporal scale to be a monthly dataset. When the ratio of valid data in each month is lower than 90%, the averaged value is taken as in-valid value. The spatial resolutions of all of the inputs were interpolated to a 0.05° spatial resolution using a widely used bilinear interpolation method.

Table 1. Input datasets used to calculate the ET on the Tibetan Plateau.

	Data source	Temporal resolution	Availability	Domain	Spatial resolution	Method
SWD	CMFD	3 h	1979–2018	China land	0.1° × 0.1°	Reanalysis
LWD	CMFD	3 h	1979–2018	China land	0.1° × 0.1°	Reanalysis
T_a	CMFD	3 h	1979–2018	China land	0.1° × 0.1°	Reanalysis
q	CMFD	3 h	1979–2018	China land	0.1° × 0.1°	Reanalysis
Wind speed	CMFD	3 h	1979–2018	China land	0.1° × 0.1°	Reanalysis
P_a	CMFD	3 h	1979–2018	China land	0.1° × 0.1°	Reanalysis
Prec	CMFD	3 h	1979–2018	China land	0.1° × 0.1°	Reanalysis
LST	ERA5	Monthly	1981–2021	Global	0.1° × 0.1°	Reanalysis
α	GLASS	8 days	1981–2019	Global	0.05° × 0.05°	Satellite
NDVI	AVHRR	Daily	1981–2019	Global	0.05° × 0.05°	Satellite
SM	GLEAM	Monthly	1979–2019	Global	0.25° x 0.25°	Reanalysis
Soil Properties	HWSD	/	/	China land	0.083°/1 km	/

2.3 Validation methods

2.3.1 Point-scale validation

The MOD16-STM model has been validated using 10 soil textures (loam, silt loam, sandy loam, sand, loamy sand, clay loam, silty clay loam, silty clay, and clay) for independent sites with three surface cover types (grassland, evergreen forest, and cropland) (Appendix A). Furthermore, the ET estimation needed to be validated through comparison with independent flux tower observations. In this study, hourly flux data measured by eddy-covariance at nine stations (Table 2) of the China-Flux (Dang-Xiong site (DX), Hai-Bei site (HB), Yu et al., 2006; Zhang et al., 2019a), the Tibetan Observation and Research Platform (TORP) (BJ, NADORS, SETORS, QOMS, NAMORS, and Shuang-Hu (SH), Ma et al., 2020), and the Heihe Water Watershed Allied Telemetry Experimental Research (HiWATER) (Arou, Liu et al., 2011, 2018; Che et al., 2019) networks, were used to validate the modeled ET. The locations of these stations had three land cover types (grassland, alpine steppe, and Gobi). It should also be noted that the energy balance closure ratio (ECR) means that the sum of sensible heat (H), latent heat (LE) and soil heat flux (G_0) does not equal net radiation (R_n). Therefore, eddy-covariance measurements should be screened and corrected beforehand. Half-hour LE data was corrected using Bowen ratio energy balance correction (Chen et al., 2014):

$$ECR = \frac{H + LE}{R_n - G_0} \tag{18}$$

$$LE_{cor} = \frac{1}{ECR} \times LE \tag{19}$$

Table 2. Details of the nine flux observation stations.

Sites	Long., Lat.	Land cover type	Elevation (m)	Availability	Climate zone	Reference
Shuang-Hu (SH)	88.83°E, 33.21°N	Alpine meadow	4947	2013–2018	Semi-arid	
BJ	91.90°E, 31.37°N	Alpine meadow	4509	2010–2016	Semi-arid	
NADORS	79.60°E, 33.38°N	Alpine steppe	4264	2010–2018	Arid	Ma et al., 2020
SETORS	94.73°E, 29.77°N	Alpine meadow	3326	2007–2018	Sub-humid	
QOMS	86.95°E, 28.35°N	Gobi	4276	2007–2018	Semi-arid	
NAMORS	90.99°E, 30.77°N	Alpine meadow	4730	2008–2018	Semi-arid	
Arou	100.46°E, 38.05°N	Alpine meadow	3033	2008–2017	Sub-humid	Liu et al., 2011, 2018; Che et al., 2019
Dang-Xiong (DX)	91.06°E, 30.49°N	Alpine meadow	2957	2004–2010	Semi-arid	Yu et al., 2006;
Hai-Bei (HB)	101.32°E, 37.61°N	Alpine meadow	3190	2002–2010	Sub-humid	Zhang et al., 2019a

To this end, the half-hourly LE_{cor} data from all the flux sites were processed to daily and monthly averaged values, using a quality control procedure. The daily average values derived from valid numbers less than 80% in one day were set as null values. Similarly, the monthly average values derived from valid numbers less than 80% in each month were also not used in the validation.

2.3.2 Accuracy evaluation metrics

The results of the long time series ET simulations are validated by comparing the pixel values (M_i) corresponding to the latitude and longitude of the flux site with the flux tower measurement (G_i). The coefficient of determination (R^2), mean bias (MB), root mean square error (RMSE), and index of agreement (IOA) were selected to assess the accuracy of the modeled ET. The equations for these parameters are as follows:

$$R^2 = \frac{\left(\sum_{i=1}^{n}(M_i - \overline{M})(G_i - \overline{G})\right)^2}{\sum_{i=1}^{n}(M_i - \overline{M})^2 \sum_{i=1}^{n}(G_i - \overline{G})^2}, 0 \le R^2 \le 1 \qquad (20)$$

$$MB = \frac{1}{N}\sum_{i=1}^{n}(M_i - G_i) \qquad (21)$$

$$RMSE = \sqrt{\frac{1}{n}\sum_{i=1}^{n}(M_i - G_i)^2} \qquad (22)$$

$$IOA = 1 - \frac{\sum_{i=1}^{n}(M_i - G_i)^2}{\sum_{i=1}^{n}(|M_i - \overline{G}| + |G_i - \overline{G}|)^2} \qquad (23)$$

where $\overline{G}$ and $\overline{M}$ are the mean flux tower and simulated ET values, respectively, the subscript i denotes the ith sample, and n is the number of samples. The R^2 value was calculated to evaluate the linear relationship between the modeled and observed ET. A higher R^2 value indicates a higher correlation. The MB was used to assess whether the result was overestimated (positive MB values) or underestimated (negative MB values). The RMSE was used to evaluate the performance of the model. A smaller RMSE indicates a higher accuracy. The IOA quantifies the degree to which the simulated ET and flux tower are correlated to each other, with values between 0 and 1.

3. Results

3.1 Evaluation of ET products against flux tower measurements

The reliability of the remote sensing-based ET estimates is questionable in the absence of verification using ground measurements. For every eddy-covariance site on the TP, we extracted the simulated monthly ET rates of the 0.05° grid where the flux tower was located. The validation results for the monthly MOD16-STM ET obtained using the flux tower observational data are shown in Fig. 3. Compared to the ET observations, the

modeled ET exhibited a good performance and high consistency over the TP. The grassland sites (SETORS, Arou, DX, and HB) performed well, with R^2 and IOA values exceeding 0.82 and 0.95. The NAMORS site performed the poorest, with the highest RMSE (17.84 mm/month) and the lowest R^2 and IOA (0.63 and 0.87, respectively). On average, the mean R^2 and IOA values were greater than 0.83 and 0.93. The R^2 values all passed the significance test at the $p < 0.05$ level. The mean |MB| and RMSE values were less than 3 mm/month and 14 mm/month. It should be noted that the fact that MB was greater than 0 revealed that the ET was overestimated, especially during the dry season over the barren land (QOMS, DX, SH, and NADORS) (Fig. 3). Fig. 4 shows the time series of the variations in the ET. In general, both the MOD16-STM ET and observed ET exhibited clear seasonal variation characteristics at the nine flux tower stations. Moreover, an annual periodic variation was observed at most stations. The overestimation at lower ET rates may be due to the fact that all ET is considered as E_s in winter, and r_s^s is underestimated which cause ET is overestimated at the same soil moisture. Conversely, underestimation occurred at larger ET rates in summer, probably because the soil was close to saturation and r_s^s was overestimated leading to an underestimation of E_s and thus ET. Overall, the site-scale validation demonstrates that the MOD16-STM ET has a satisfying accuracy in the TP region.
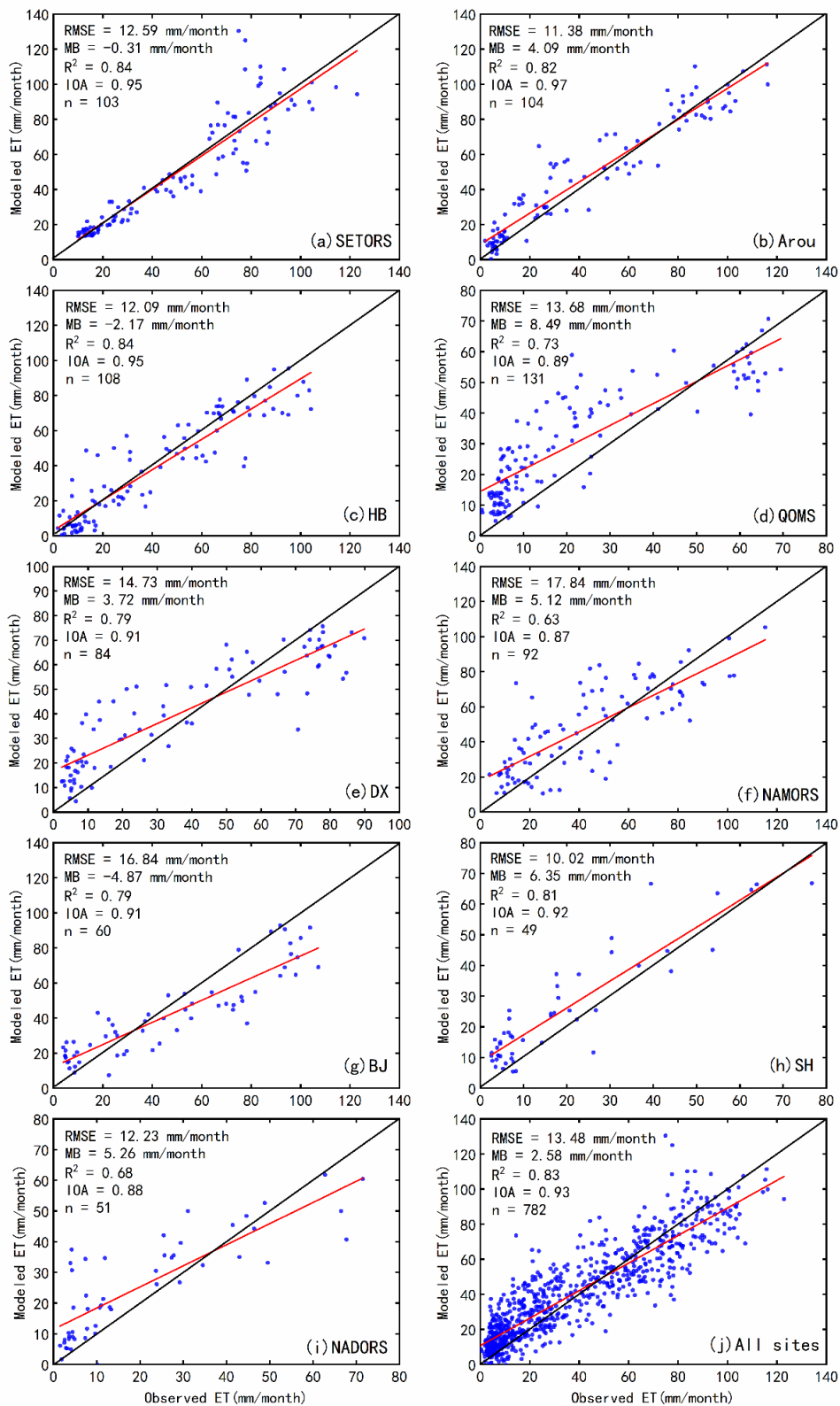
Figure 3 The validation of the MOD16-STM monthly ET at (a) SETORS, (b) Arou, (c) HB, (d) QOMS, (e) DX, (f) NAMORS, (g) BJ, (h) SH, (i) NADORS, and (j) all sites.
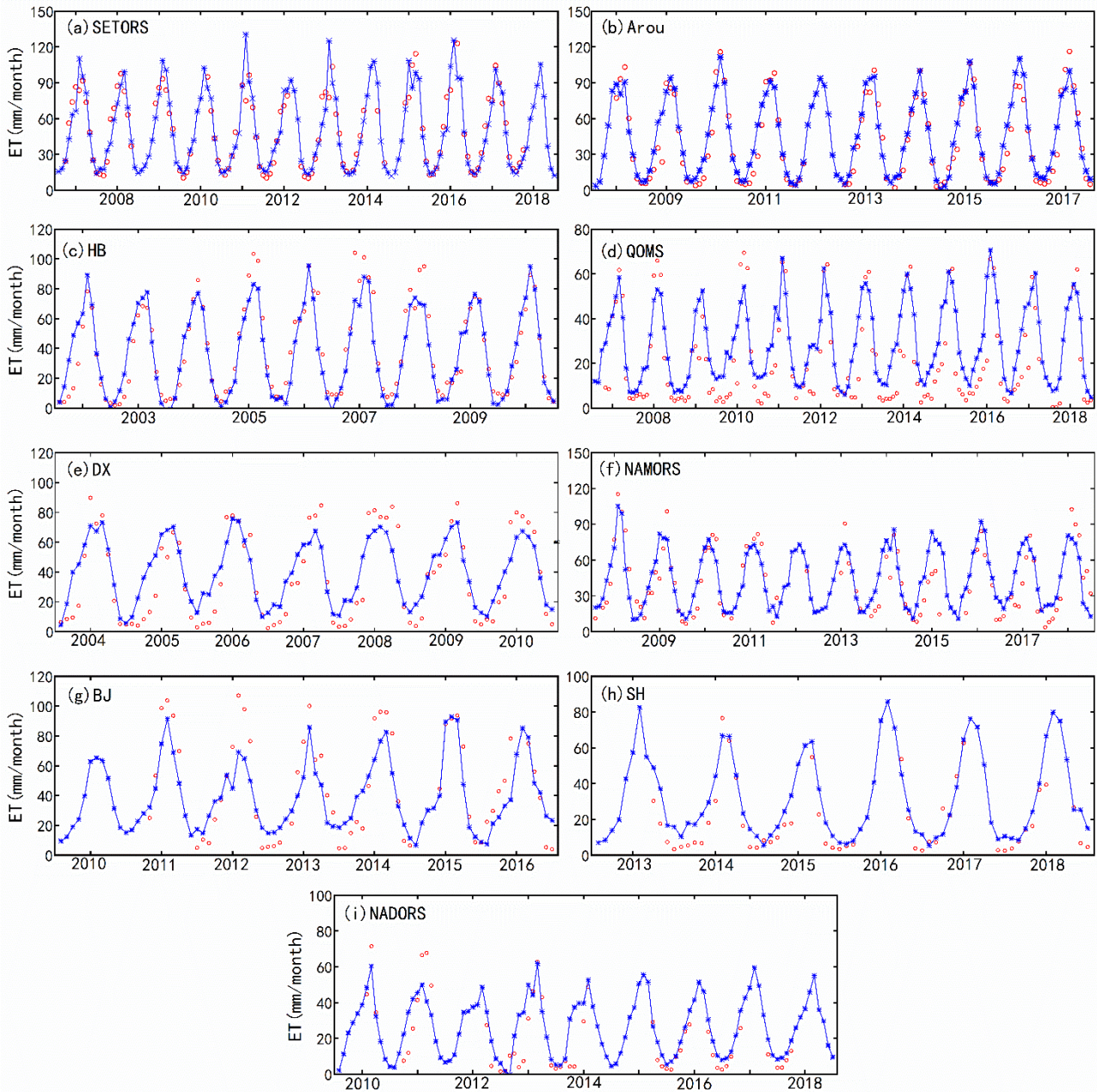
Figure 4 Time series variations in the MOD16-STM simulated ET (blue solid line with '*' marks) and flux-tower-observed ET (red circles) at (a) SETORS, (b) Arou, (c) HB, (d) QOMS, (e) DX, (f) NAMORS, (g) BJ, (h) SH, and (i) NADORS.

3.2 Spatial pattern of the multiyear averaged ET across TP

Fig. 5 shows the spatial pattern of the average annual ET and its three components across the TP. The ET decreased from southeast to northwest, with the maximum values exceeding 1000 mm/year on the southeastern Tibetan Plateau (the Heng-duan Mountains) and minimum values of less than 100 mm/year in the Qaidam Basin and northwestern TP. The spatial pattern of the annual ET was consistent with that of the aridity index (AI) (Fig.

1b), which is due to the combined effect of the atmospheric demand and water supply. The ET of the sub-humid zone (32.9% of the TP) contributed the highest percentage (43% of the TP's ET) compared to the other climate zones. The E_s obviously dominated on the central and western TP, and its spatial distribution pattern was quite similar to that of the ET. The spatial distributions of the E_c and E_w were consistent with the spatial distribution of the vegetation. The high E_c (>200 mm/year) and E_w (>50 mm/year) values were mainly concentrated in the densely vegetated areas of the Heng-duan Mountains on the southeastern TP.

The multiyear-average ET in spring (March, April, and May), summer (June, July, and August), autumn (September, October, and November), and winter (December, January, and February) on the TP are shown in Fig. 6. The estimated ET seems to capture the general pattern of the seasonal cycles relatively well. The average ET was higher in spring than in autumn. The ET ranged from 20 to 250 mm in spring and from 20 to 150 mm in autumn. This is attributed to the fact that as the ground surface increases with increasing temperature in spring, more free surface water is generated via thawing of the permafrost and melting of snow and ice, which enhances the surface evaporation processes. In addition, vegetation transpiration increases during the growing season. In summer, the ET is greater than 200 mm over most of the TP, but the ET is still less than 100 mm in large areas of the northwestern TP. However, lower ET values were only observed in the densely vegetated southeastern region of the TP in winter due to the lower amount of available water (precipitation) and lower Ta throughout the entire TP.

The multi-year average land surface ET over the TP was 346.5 ± 13.2 mm/year (mean ± standard deviation, the latter represents the interannual variability) (about 0.88 ± 0.034 Gt/year), with E_s equal to 292.36 ± 10.39 mm/year (0.74 ± 0.027 Gt/year), E_c equal to 47.85 ± 3.34 mm/year (0.12 ± 0.006 Gt/year), and E_w equal to 7.07 ± 2.89 mm/year (0.02 ± 0.001 Gt/year). The multi-year mean annual E_s accounted for the majority of the ET on the TP (more than 84%). Wang et al. (2020) accurately calculated the amount of water evaporated from all of the plateau lakes, i.e., 0.0517 Gt/year. Thus, using the area-weighted average method, the average annual water evaporated on the entire TP was about 0.93 ± 0.037 Gt/year. The average annual rainfall on the TP is about 1.8 × 10^3 Gt/year, estimated from the data of ERA5-Land, CMFD, and TPHiPr in Jiang et al., 2022. About 53% of the precipitation on the TP returns to the atmosphere through ET. The multiyear seasonal ET averaged over the entire TP is 90.79 ± 3.16 mm/year (0.23 ± 0.0081 Gt/year), 152.05 ± 8.44 mm/year (0.38 ± 0.021 Gt/year), 71.96 ± 2.86 mm/year (0.18 ± 0.0074 Gt/year), and 30.54 ± 1.85 mm/year (0.077 ± 0.0047 Gt/year) in spring, summer, autumn, and winter, respectively.
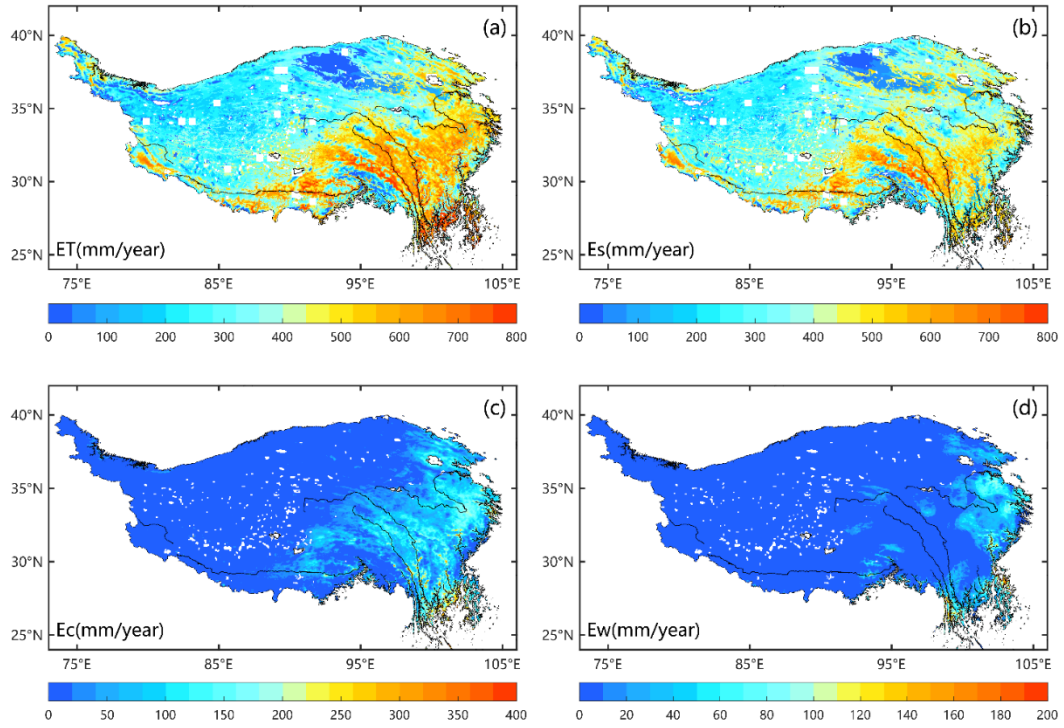
Figure 5 Spatial pattern of the multiyear (1982–2018) mean annual (a) ET (evapotranspiration), (b) E_s (soil evaporation), (c) E_c (canopy transpiration), and (d) E_w (intercepted water evaporation) across the Tibetan Plateau.
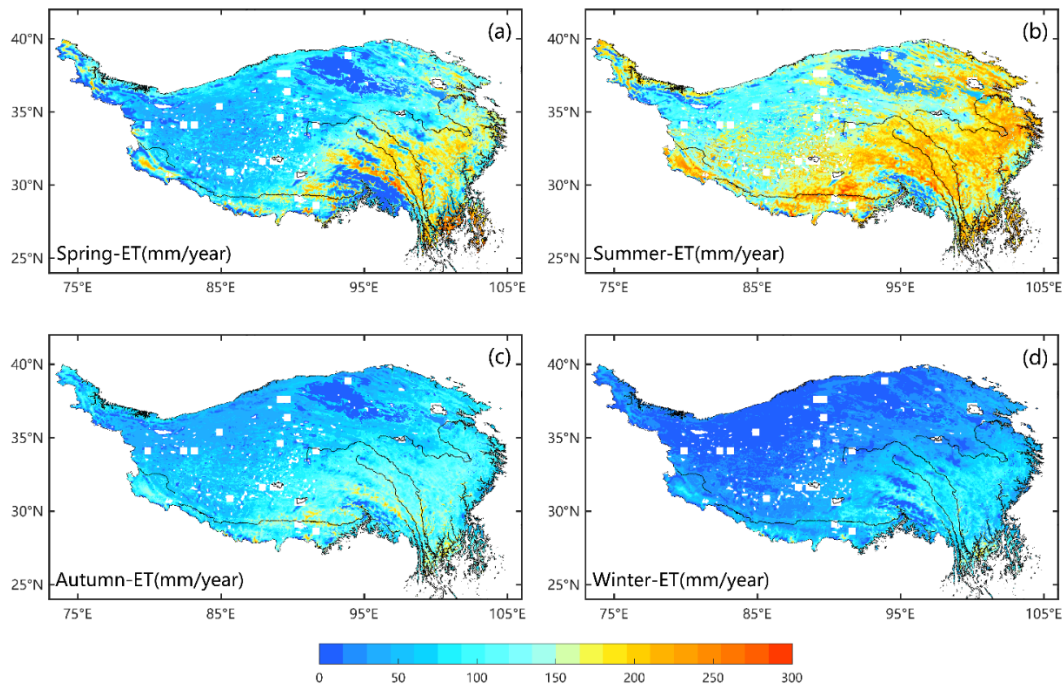
Figure 6 Spatial distributions of the multiyear (1982–2016) mean seasonal ET in (a) Spring, (b) Summer, (c) Autumn, and (d) Winter across the Tibetan Plateau.

3.3 Temporal variations in ET across TP

Quantifying the inter- and intra-annual variations in the ET is important in studying monsoon phenomena and climate change on the TP. Figure 7 shows the spatial patterns of the annual ET and its component trends during 1982–2018. The trends of the ET are spatially heterogeneous over the TP. The annual ET significantly increased, with rates of about 1–4 mm/year ($p<0.05$), over most parts of the central and eastern TP, accounting for more than 86% of the TP. However, it significantly decreased, with rates of −3 to −1 mm/year, on the northwestern TP. In addition, the E_s rates exhibited a spatial distribution similar to that of the ET, and the increasing trends had lower magnitudes (1–3 mm/year, $p<0.05$). Both the E_c and E_w exhibited slightly increasing trends of 0–2 mm/year ($p<0.05$). Averaged across the entire TP, the ET, E_s, and E_c increased significantly during 1982–2018, with rates of 0.96 mm/year, 0.64 mm/year, and 0.44 mm/year, respectively ($p<0.05$; Fig.8). Regarding the seasonality, the seasonal ET trends were positive and significant in all of the seasons (Fig.8). The strongest trends occurred in summer (0.46 mm/year). In addition, the multi-source ET products indicate that most of the regions of the TP exhibited consistent ET changes over the past 30 years (Yin et al., 2013; Peng et al., 2016; Wang et al., 2018; Ma et al., 2019; Wang et al., 2020; Li et al., 2021; Ma et al., 2022).
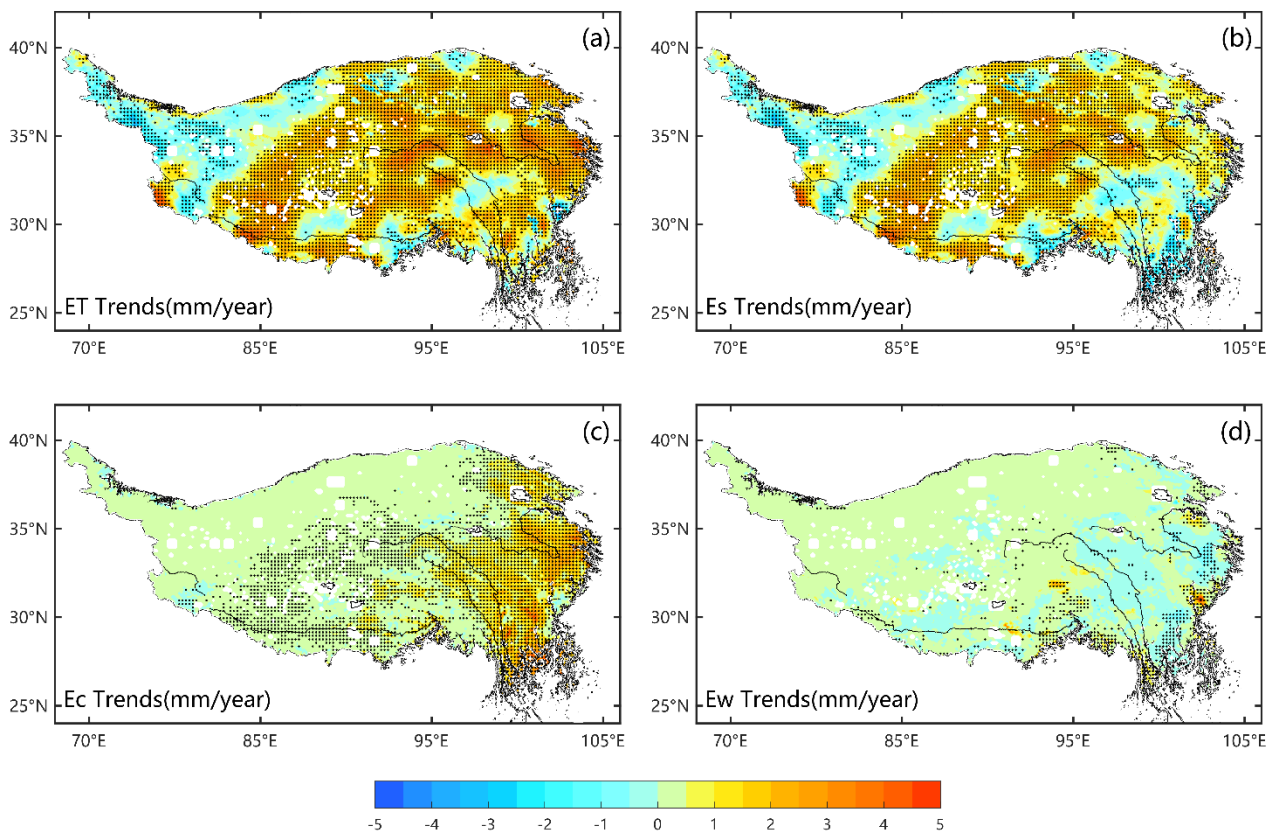

Figure 7 Spatial patterns of the trends (1982–2018) of the annual (a) ET (evapotranspiration), (b) E_s (soil evaporation), (c) E_c (canopy transpiration), and (d) E_w (intercepted water evaporation) across the Tibetan Plateau. The stippling on the maps indicates the trends that are statistically significant ($p<0.05$).
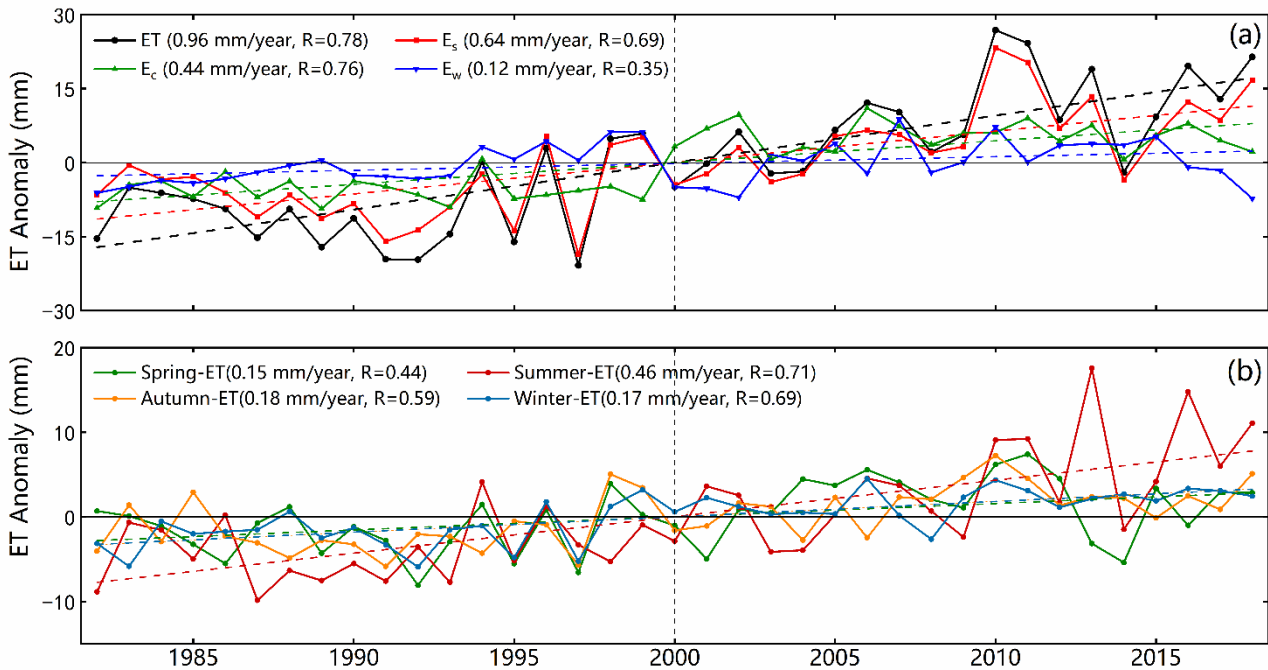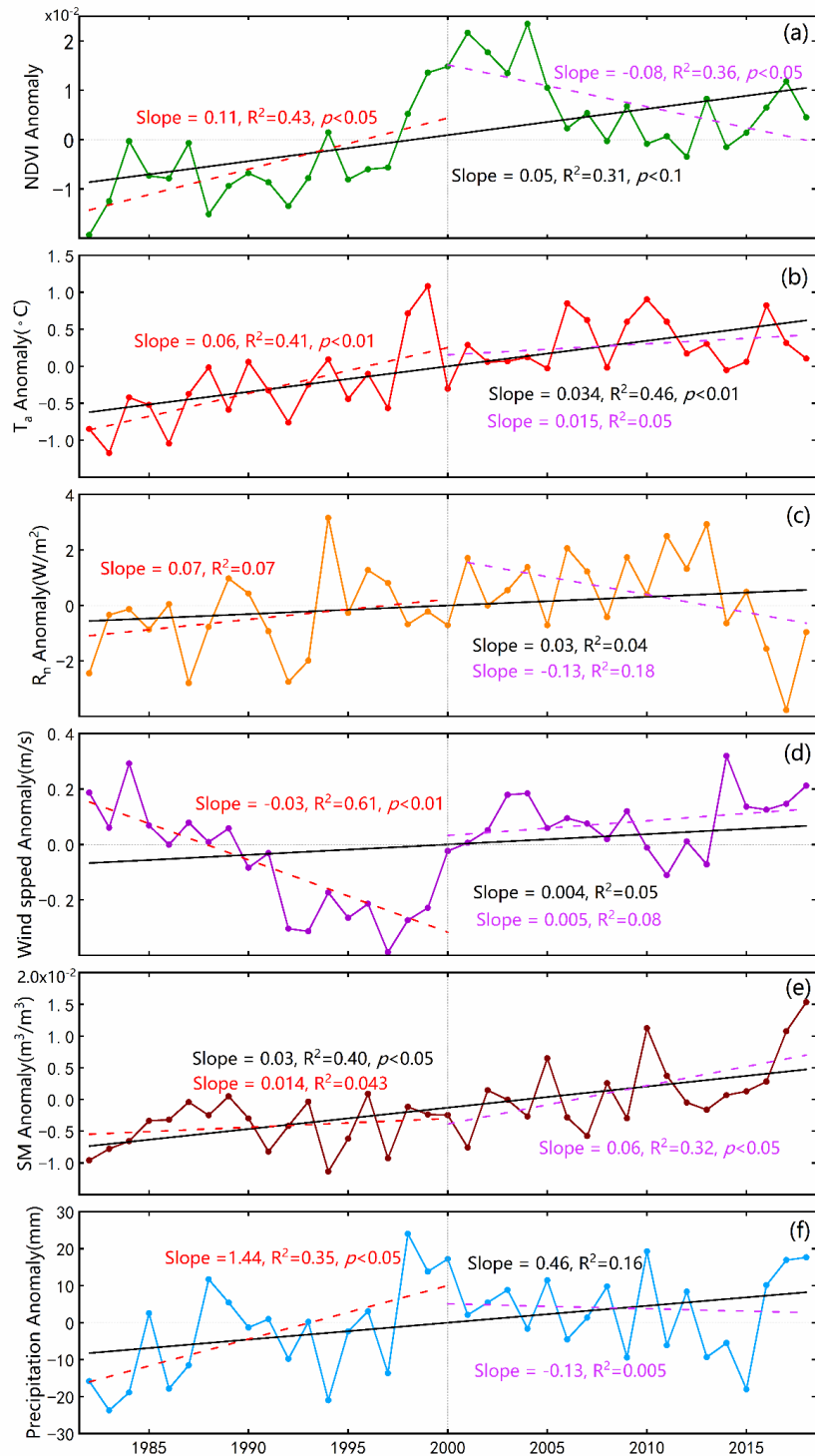
Figure 8 Time series of the (a) anomalies in the annual ET and its three components, and (b) anomalies in seasonal mean ET. The least squares fitted linear trend were demonstrated by the dashed colored lines.

The increase in the ET over the entire TP from 1982 to 2018 can be explained by the warming and wetting of the climate on the TP during this period. Since the 1980s, the TP has experienced overall greening, warming, and wetting (increased soil moisture and precipitation) (Fig.9). The ET has continuously increased in the past 40 years, while the changes in the climate factors shifted significantly in the middle of this time period (around 2000). From 1982 to 2000, the ET continuously increase, the wind speed rapidly decreased, and did not change the Rn significantly. There was a rapid decrease in the Rn and no significant change in the wind speed from 2000 to 2018, while the ET continued to increase during this period. Therefore, the Rn and wind speed were not the dominant factors controlling the annual variations in the ET. The significant increases in the T_a, SM, and precipitation were accompanied by greening of the land surface in the last two decades. Together, these factors led to an increase in the ET. In the latest ten years, only the significant growth of the SM controlled the growth of the ET.

In general, the increase in ET over the TP was due to the increase in the available surface water during the entire study period. There is also evidence that an overall increase in precipitation occurred across the TP. The combined effect of the warming and vegetation greening led to further opening of the vegetation stomata. The more favorable vegetation conditions explain the increase in the vegetation transpiration. The warming of the

land surface and increased wind speeds led to more efficient turbulent water exchange between the land and atmosphere. In addition, the warming accelerated the melting of the permafrost and glaciers on the TP. Due to the wetting of the surface and the thickening of the active soil layer, water could be transported more easily from the lower layer to the upper soil layer.

Figure 9 Time series of the annual anomalies in the (a) NDVI, (b) Ta, (c) Rn, (d) u, (e) SM, and (f)

precipitation and their least squares fitted linear trends during two periods of 1982-2000 and 2000-2018.

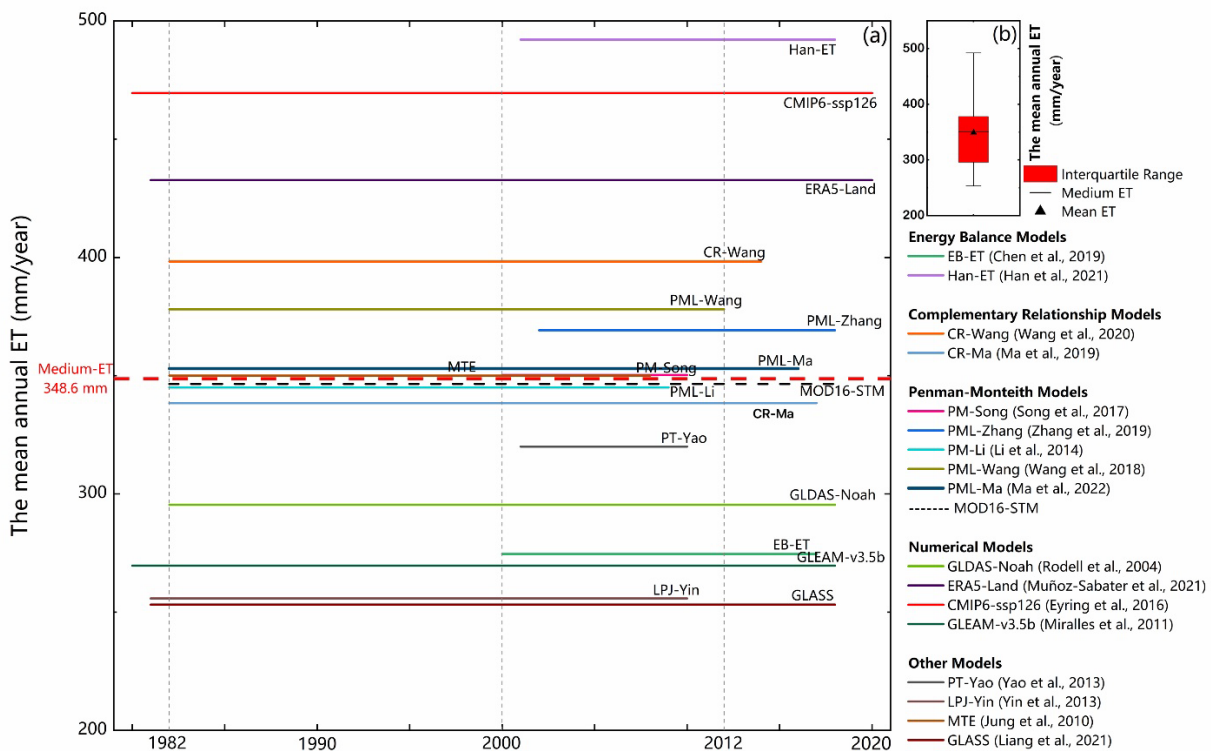### 3.4 Comparison of the MOD16-STM product to other ET product over the TP

The MOD16-STM ET had a relatively good performance on the TP overall, with an average R^2 value of 0.83 and an average RMSE of 13.48 mm/month. These results are close to those obtained in other studies. Wang et al. (2018) evaluated the performance of a modified PML model for ET estimation (PML-Wang) on the TP. Their results yielded R^2 values > 0.85 and RMSE values < 14 mm/month. The spatially averaged ET during 1982–2012 was 378.1 mm/year. Wang et al. (2020) evaluated the performance of the generalized nonlinear complementary principle for ET estimation (CR-Wang) based on flux tower observation data from the TP. Their results showed that the R^2 increased from 0.87 to 0.93, and the RMSE decreased from 0.53 to 0.40 mm/day. The spatially averaged ET during 1982–2014 was 398.3 mm/year. Han et al. (2021) used an algorithm of the effective aerodynamic roughness length coupled with the SEBS model to estimate the ET for the entire TP from 2001 to 2018 (Han-ET). They found that the modeled value was consistent with the in situ measured value (R^2 > 0.81, RMSE < 14.5 mm/month), and the average annual ET is around 496 ± 23 mm on the TP, which was higher than 346.5 ± 13.2 mm obtained in this study. This discrepancy is mainly due to the different models and time periods of the two studies. Ma et al. (2022) used PML_V2 to estimate the ET on the TP (PML-Ma), and their R^2 and RMSE values varied from 0.4 to 0.9 and from 0.3 to 0.8 mm/day, respectively. The 35-year mean annual ET rates from PML-Ma led to an average value of 353 ± 24 mm/year for the entire TP. Soil evaporation is about 64% of the ET, estimated from PML-Ma, which is lower than the estimated 84% in this study. The main reason for the ratio difference is maybe because of the differences in the land cover classification. The land cover of the MODIS largely classifies the land surface of the northwestern TP as bare soil, which leads to an increase in the proportion of soil evaporation.

4. Discussion

4.1 Discrepancy on the estimation of annual ET over the TP

Fig. 10 demonstrates the time period covered by each ET dataset and their annual ET estimations for the TP. Yao et al. (2013) estimated the ET (PT-Yao) in China using a satellite-driven modified Priestley–Taylor algorithm, which is constrained by the NDVI and the apparent thermal inertia derived from the temperature changes over time, and they reported that the mean annual ET on the TP was about 320 mm/year. Song et al. (2017) estimated TP's ET (PM-Song) using the improved Penman–Monteith method and meteorological and satellite remote sensing data with a spatial resolution of 1 km during 2000–2010, and they concluded that the average annual ET on the TP was 350.3 mm/year. In addition to this, the 18 mean annual ET values estimated

using existing ET products (PML-Zhang (Zhang et al., 2019b), EB-ET (Chen et., 2019, 2021), CR-Ma (Ma et al., 2019), CMIP6-ssp126 (Eyring et al., 2016), GLDAS-Noah (Rodell et al., 2004), GLASS (Liang et al., 2021), GLEAM-v3.5b (Miralles et al., 2011), and ERAR-Land (Muñoz-Sabater et al., 2021), MTE (Jung et al., 2010), PM-Li (Li et al., 2014a), LPJ-Yin (Yin et al., 2013)) were also demonstrated. The Han-ET, ERA5-Land, and CMIP6 produced the highest values (>400 mm/year), while the LPJ-Yin, GLASS, EB-ET, GLDAS, and GLEAM values were less than 300 mm/year. The results show a large difference exist in the estimated mean annual ET values for the TP. The differences in these results are partially caused by objective factors such as the inaccuracy of the input data and the limitations of the validation methods. In addition, the subjective factor of the algorithm's flaw can also led to additional biases. The medium value of the annual ET from an ensemble of all the datasets is 348.6 mm/year. MOD16-STM model estimation (346.5 mm/year) is the closest to the ensemble mean. Overall, the MOD16-STM ET exhibited acceptable performance on the TP again.

Figure 10 (a) The annual mean ET values of 18 datasets. The *x*-axis is the time coverage of the ET datasets, and the *y*-axis is the multi-year mean value. (b) The bars denote the mean values and variations of the annual ET.

4.2 Errors caused by objective factors

The MOD16-STM and other models use remote sensing data and reanalysis data as the main input data.

420 However, the accuracy of these data is somewhat uncertain (Ramoelo et al., 2014). For instance, the topsoil water content is a critical radiative parameter; however, complex algorithm led reanalysis data contain errors in its SM simulation. Liu et al. (2021) reported that the long-term GLEAM SM product based on a satellite-based input dataset yields limited improvement in its SM outputs. A large number of studies have already reported that the TP is becoming greener. In Fig. 9a, NDVI decreases significantly after 2000, while warming and wetting

425 can still be seen during this period, which is quite different from the NDVI changes studied by Wang et al. (2022). Therefore, there is still great uncertainty in the driving data. Furthermore, as a fundamental parameter in the calculation of the surface energy balance, the LST affects the estimation of the ET to a great extent (Long et al., 2011). In this study, we used an NDVI threshold to divide when the land surface can be taken as bare soil or canopy covered pixel. The mismatch between the in-homogeneous underlying surface and the land surface

430 types in the MOD16-STM ET can also lead to errors. In general, the flux towers covered areas ranging from a few hundred square meters to several square kilometers, depending on the height of the observation instrument, the turbulence intensity, topography, environment, and vegetation conditions. Although site scale evaluations of the MOD16-STM ET were performed in this study, the uncertainties arising from the limited number of validation sites should be noted, and validation with different land cover types, climate zones, elevations, and

435 seasons should be considered further in future.

Although the MOD16 model directly estimates ET, avoiding the process of calculating sensible heat. The empirical coefficients for the different soil textures were redefined. There are still some empirical parameters (e.g., C_L, the mean potential stomatal conductance per unit leaf area) that can increase the uncertainty of the simulation results. Therefore, it is necessary to parameterize these empirical parameters according to physical

440 processes to reduce the uncertainty of the simulation results in future studies. The influence of the physical processes of deeper soil water and heat transfer on the resistance should be considered. The MOD16-STM algorithm has a great dependence on higher-precision soil moisture products. Most areas of the TP are covered by permafrost and seasonally frozen soil. It is difficult to grasp the SM conditions during the soil freezing and thawing period. Therefore, it is necessary to use observations during the soil freeze-thaw period to verify the

445 applicability of the model.

5. Conclusion

In this study, we developed a 37-year (1982–2018) monthly ET dataset with a 0.05° spatial resolution for the TP using the newly developed MOD16-STM model coupled with soil information to investigate the spatial

distribution and temporal trends of the ET on the TP. This dataset covers the full study area with a high spatial resolution and a long time period. It is a suitable ET database for climate studies. Main findings are summarized below.

1. The ET product generated using MOD16-STM exhibited a good performance on the TP. Compared to the flux tower observation data, the R^2 and IOA values of the modeled ET reached 0.83 and 0.93, with the RMSE of 13.48 mm/month and an MB of 2.58 mm/month. This ET data can be used in water resource management, drought monitoring, and ecological studies.

2. The combined effect of the atmospheric demand and water supply resulted in spatial heterogeneity of the ET and the temporal changes in the ET. The annual ET generally decreased from southeastern to northwestern of the TP. The E_s accounted for more than 84% of the annual ET. The estimated multiyear (1982–2018) mean annual ET on the TP was 346.5±13.2 mm, approximately 0.93 ± 0.037 Gt/year water evaporated from the entire TP.

3. The ET exhibited a significant increasing trend, with rates of about 1 to 4 mm/year ($p<0.05$), over most parts of the central and eastern TP, while the northwestern TP demonstrate a decreasing trend of -3 to -1 mm/year ($p<0.05$). Averaged across the entire TP, the ET increased significantly during 1982–2018, with a rate of 0.96 mm/year ($p<0.05$). The increase in the ET over the entire TP from 1982 to 2018 can be explained by the warming and wetting of the climate during this period.

Data availability

The monthly ET dataset presented and analyzed in this article has been released and is freely available at the Science Data Bank (http://doi.org/10.11922/sciencedb.00020, Y. Ma*, X.Chen*, L. Yuan, 2021) and the National Tibetan Plateau Data Center (TPDC) (https://data.tpdc.ac.cn/en/disallow/e253621a-6334-4ad1-b2b9-e1ce2aa9688f/, http://doi.org/10.11888/Terre.tpdc.271913, L. Yuan, X.Chen*, Y. Ma*, 2021). The dataset is published under the Creative Commons Attribution 4.0 International (CC BY 4.0) license.

Author contributions

YMM, LY, and XLC led the writing of this paper and acknowledge responsibility for the experimental data and results. LY and YMM drafted the paper, and LY led the consolidation of the input and simulation dataset. XLC revised the manuscript. This paper was written in cooperation with all of the co-authors.

Appendix A: MOD16-STM Validation at flux site out of the Tibetan Plateau

Table A1. Basic Information about the five test sites and 12 verification sites.

	Site	Lat; lon	Land cover	θ (cm)	f_{sand}	f_{clay}	m_{soc} (%)	θ_{sat}	Soil Texture	Reference
Test Sites	IT-Cas	45.07; 8.71	CRO	5	0.28	0.29	2.6	/	Clay loam	*Denef et al. (2013)*
	US-IHO	36.47; 100.62	Bare	5	0.58	0.28	/	0.53	Sandy Clay Loam	*Lemone et al.* (2007)
	US-Arm	36.61; -97.49	CRO	5	0.28	0.43	1.5	/	Clay	*Fischer et al.* (2007)
	CH-Oe2	47.29; 7.73	CRO	5	0.095	0.43	2.8	/	Silty Clay	*Alaoui and Goetz (2008)*
	US-IB2	41.84; -88.24	GRA	0~15	0.106	0.29	2.4	/	Silty clay Loam	/
Independent verification sites	US-Dk1	35.97; -79.09	GRA	10	0.48	0.09	/	0.52	Loam	*Novick et al. (2004)*
	US-Fwf	35.45; -111.77	GRA	5	0.30	0.13	3.2	/	Silt Loam	*Dore et al. (2012)*
	US-Wkg	31.74; -109.94	GRA	5	0.67	0.17	1.0	/	Sandy Loam	*Ameri-Flux*
	CA-Obs	53.98; -105.11	ENF	5	0.72	0.05	4.3	/	Sandy Loam	*Ameri-Flux*
	CA-Ojp	53.91; -104.69	ENF	5	0.94	0.03	2.5	/	Sand	*Ameri-Flux*
	CA-Ca2	49.87; -125.29	ENF	5	0.74	0.03	3.0	/	Loamy Sand	*Ameri-Flux*
	CA-Ca3	49.53; -124.90	ENF	5	0.39	0.20	4.9	/	Loam	*Ameri-Flux*
	US-Dk3	35.97; -79.09	ENF	5	0.25	0.34	2.4	/	Silt Loam	*Ameri-Flux*
	US-Fuf	35.08; -111.76	ENF	5	0.31	0.35	3.9	/	Clay Loam	*Ameri-Flux*
	US-Ib1	41.86; -88.22	CRO	2.5	0.10	0.35	1.8	/	Silty clay Loam	*Denef et al. (2013)*
	ES-ES2	39.28; -0.32	CRO	5	0.11	0.47	3.7	/	Silty Clay	*Kutsch et al. (2010)*
	IT-Bci	40.52; 14.96	CRO	5	0.32	0.46	1.5	/	Clay	*Denef et al. (2013)*
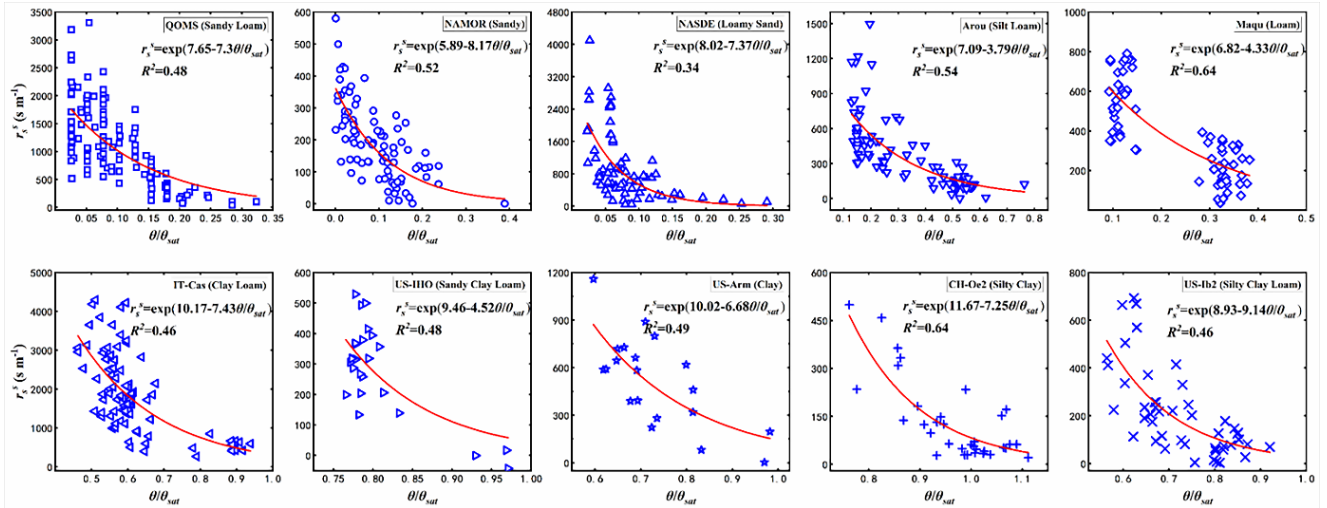
Figure A1. Soil surface resistance (r_s^s) related to the topsoil SM measured for the different soil textures (θ_{sat}): sandy loam (QOMS), sandy (NAMOR), loamy sand (NASDE), silt loam (Arou), loam (Maqu), clay Loam (IT-Cas), sandy clay loam (US-IHO), clay (US-Arm), silty clay (CH-Oe2), and silty clay loam (US-Ib2).

Table A2. Equation coefficient values for the surface soil resistances from the regressions between these resistances and the SM for the different soil textures (θ_{sat}).

Texture	$r_s^s = \exp\left(a + b \times \dfrac{SM}{\theta_{sat}} \right)$		R^2
	a	b	
Sandy Loam	7.65	-7.3	0.48
Sand	5.89	-8.17	0.52
Loamy Sand	8.02	-17.37	0.34
Silt Loam	7.09	-3.79	0.54
Loam	6.82	-4.33	0.64
Clay Loam	10.17	-7.43	0.46
Sandy Clay Loam	9.46	-4.52	0.48
Clay	10.02	-6.68	0.49
Silty Clay	11.67	-7.25	0.64
Silty Clay Loam	8.93	-9.14	0.46

545
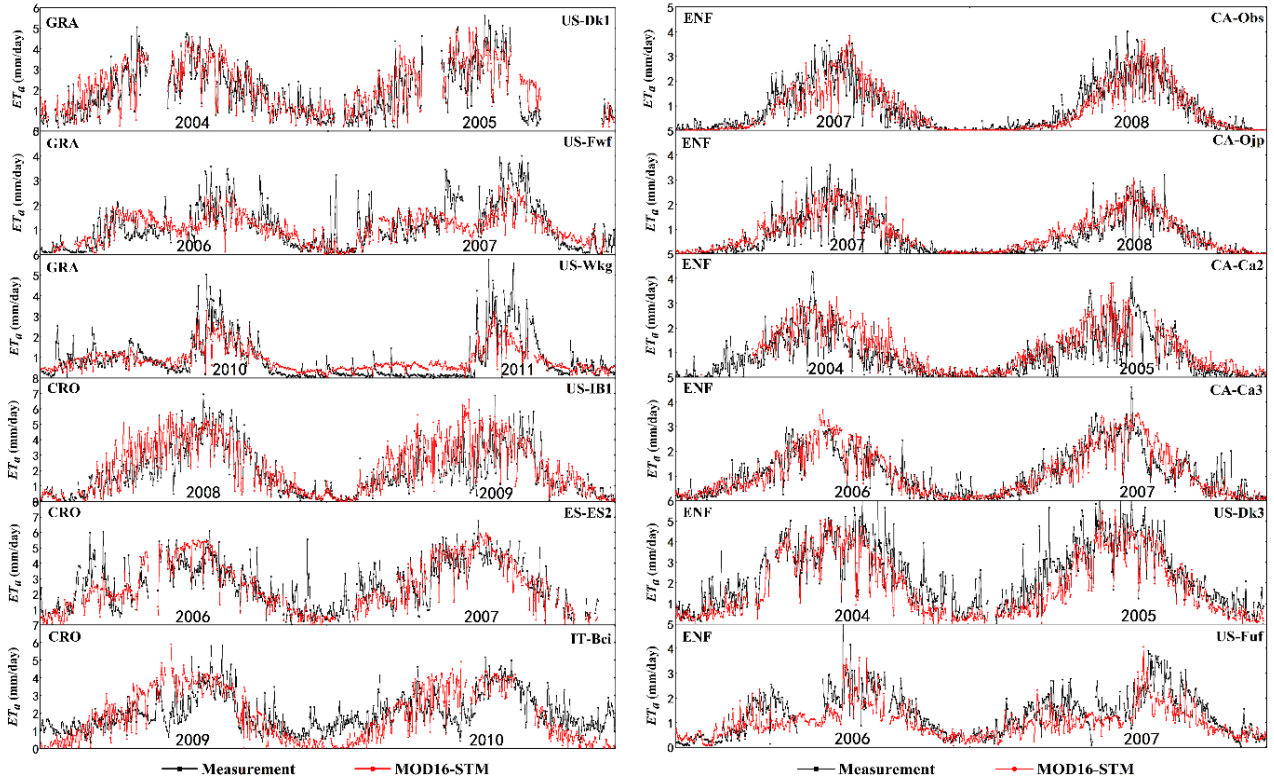
Figure A2. Time-series comparisons of the ET estimated using the MOD16-STM model and the daily flux tower observations in the grassland (US-DK1, US-Fwf, and US-Wkg), cropland (US-IB1, ES-ES2, and IT-Bci), and evergreen forest (CA-Obs, CA-Ojp, CA-Ca2, CA-Ca3, US-DK3, and US-Fuf) ecosystems.

Table A3. Statistical comparison of the daily ET (mm/day) estimated using the MOD16-STM model and daily flux tower observation data.

	Sites	R^2 ($p<0.05$)	IOA	|MB|	RMSE
Grassland	US-DK1	0.71	0.91	0.27	0.74
	US-Fwf	0.59	0.84	0.06	0.55
	US-Wkg	0.69	0.84	0.005	0.58
Evergreen Forest	CA-Obs	0.88	0.96	0.05	0.33
	CA-Ojp	0.79	0.93	0.11	0.38
	CA-Ca2	0.77	0.92	0.23	0.49
	CA-Ca3	0.79	0.94	0.02	0.44
	US-Dk3	0.79	0.92	0.51	0.87
	US-Fuf	0.58	0.81	0.33	0.66
Cropland	US-Ib1	0.65	0.88	0.39	1.08
	ES-ES2	0.87	0.91	0.04	0.94
	IT-Bci	0.41	0.76	0.14	1.14
Mean	/	0.72	0.89	0.18	0.68

570

575
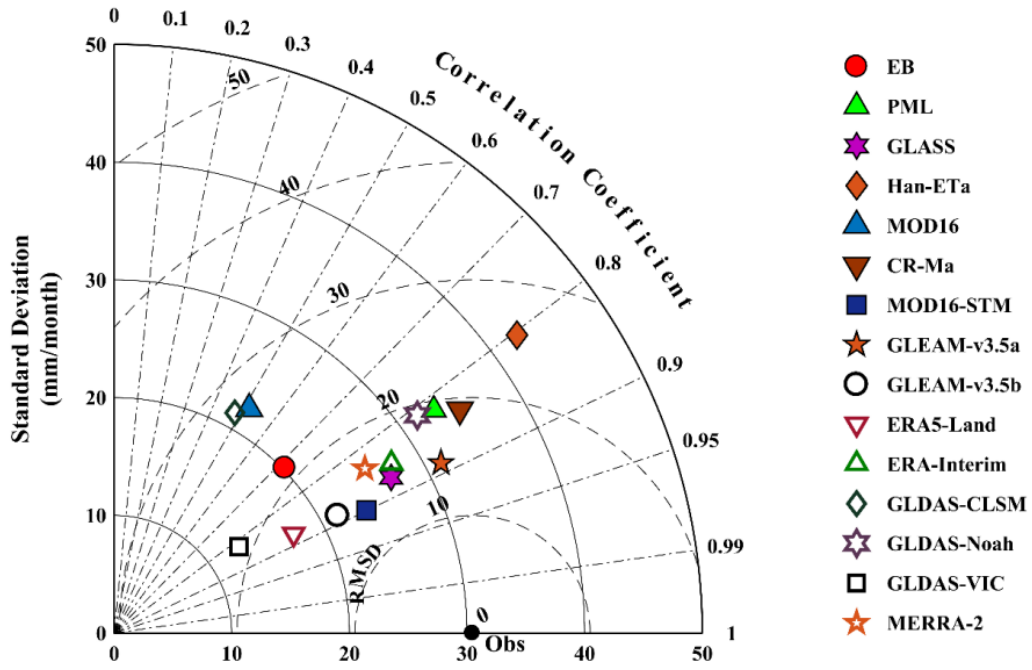
Figure A3. Taylor diagram of the monthly-scale evapotranspiration dataset validated with flux evapotranspiration observations.
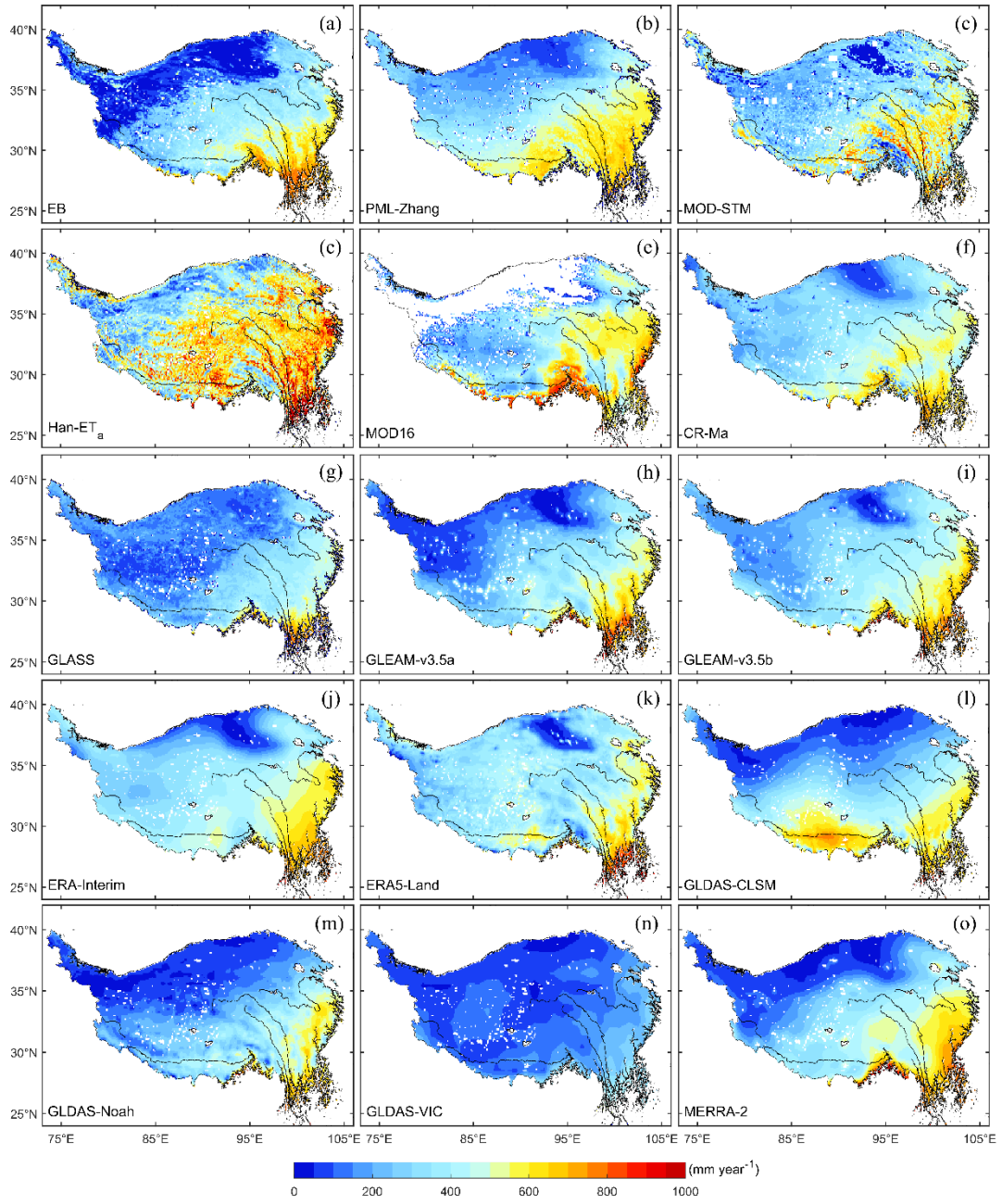
Figure A4 Spatial distribution of 15 annual mean evapotranspiration on the Tibetan Plateau from 2000 to 2014.

600

605

Symbol	Description	MOD16	MOD16-SMT
C_L	The mean potential stomatal conductance per unit LAI	0.007	0.0038
h_c	Vegetation height	Not used	In situ
ν	Kinematic viscosity of the air	Not used	$1.328 \times 10^{-5} \times \left(\dfrac{P_0}{P}\right)\left(\dfrac{T_{air}}{T_0}\right)^{1.754}$, $P_0 = 101.3$ kPa and $T_0 = 273.15$ K
u_*	Friction velocity	Not used	In situ
L	The Obukhov length (m)	Not used	In situ
T_*	Friction temperature	Not used	$\dfrac{T_{air}u_*^2}{\text{kgL}}$
z_{0h}	Heat roughness length	Not used	$\dfrac{70\nu}{u_*}\exp\left(-7.2u_*^{0.5}\left|T_*\right|^{0.25}\right)$
z_{0m}	Momentum roughness length	Not used	$h_c/8$
r_s^s	Surface resistance of bare soil	r_{tot}	$\exp\left(A + B \times \dfrac{\theta}{\theta_{sat}}\right)$
r_a^s	Aerodynamic resistance of soil surface	$r_a = \dfrac{rh \times rr}{rh + rr}$	$\dfrac{\ln\left(\dfrac{z_h}{z_{0h}} - \psi_h\right)\ln\left(\dfrac{z_m}{z_{0m}} - \psi_m\right)}{k^2 u}$
θ_{sat}	Soil porosity	Not used	$\left(1 - V_{SOC} - V_g\right) \times \theta_{sat,m} + V_{SOC} \times \theta_{sat,sc}$
$\theta_{sat,sc}$	The porosity of the SOC	Not used	$0.489 - 0.00126 \times \%\text{sand}$
V_{SOC}	Volumetric content of the SOC	Not used	$\dfrac{\rho_p \times \left(1 - \theta_{sat,m}\right) \times m_{SOC}}{\rho_{SOC} \times \left(1 - m_{SOC}\right) + \rho_p \times \left(1 - \theta_{sat,m}\right) \times m_{SOC} + \left(1 - \theta_{sat,m}\right) \times \dfrac{\rho_{SOC} \times m_g}{1 - m_g}}$
V_g	Volumetric content of gravel	Not used	$\dfrac{\rho_{SOC} \times \left(1 - \theta_{sat,m}\right) \times m_g}{\left(1 - m_g\right) \times \left(\rho_{SOC} \times \left(1 - m_{SOC}\right) + \rho_p \times \left(1 - \theta_{sat,m}\right) \times m_{SOC} + \left(1 - \theta_{sat,m}\right) \times \dfrac{\rho_{SOC} \times m_g}{1 - m_g}\right)}$

Figure A5 Comparison of Improved Parameters or Intermediate Variables in the MOD16-SMT Model and the MOD16 Model (Yuan et al., 2021).

610

615

620

References

Alaoui, A., and Goetz, B.: Dye tracer and infiltration experiments to investigate macropore flow, Geoderma., 144(1–2), 279–286, https://doi.org/10.1016/j.geoderma.2007.11.020, 2008.

Baik, J., Liaqat, U. W., and Choi, M.: Assessment of satellite- and reanalysis-based evapotranspiration products with two blending approaches over the complex landscapes and climates of Australia, Agric. For. Meteorol., 263, 388–398. https://doi.org/10.1016/j.agrformet.2018.09.007, 2018.

Bibi, S., Wang, L., Li, X., Zhou, J., Chen, D., Yao, T.: Climatic and associated cryospheric, biospheric, and hydrological changes on the Tibetan Plateau: a review, Int. J. Climatol., 38, 1-17, https://doi.org/10.1002/joc.5411, 2018.

Biermann, T., Babel, W., Ma, W., Chen, X., Thiem, E., Ma, Y., Foken, T.: Turbulent flux observations and modelling over a shallow lake and a wet grassland in the Nam Co basin, Tibetan Plateau, Theor. Appl. Climatol., 116(1–2), 301–316, https://doi. org/10.1007/s00704-013-0953-6, 2014.

Blyth, E., and Harding, R. J.: Methods to separate observed global evapotranspiration into the interception, transpiration and soil surface evaporation components, Hydrol. Process., 25(26), 4063–4068, https://doi.org/10.1002/hyp.8409, 2011.

Chang, Y., Qin, D., Ding, Y., Zhao, Q., Zhang, S: A modified MOD16 algorithm to estimate evapotranspiration over alpine meadow on the Tibetan Plateau, China, J. Hydrol., 561: 16–30, https://doi.org/10.1016/j.jhydrol.2018.03.054, 2018.

Chen, D., Xu, B., Yao, T., Guo, Z., Cui, P., Chen, F., Zhang, R., Zhang, X., Zhang, Y., Fan, J., Hou, Z., Zhang, T.: Assessment of past, present and future environmental changes on the Tibetan Plateau, Kexue Tongbao/Chinese Science Bulletin, 60(32), 3025–3035, https://doi.org/10.1360/N972014-01370, 2015.

Chen, X., Massman, W. J., Su, Z.: A Column Canopy-Air Turbulent Diffusion Method for Different Canopy Structures, J. Geophys. Res. Atmos., 124(2), 488–506, https://doi.org/10.1029/2018JD028883, 2019.

Chen, X., Su, Z., Ma, Y., Liu, S., Yu, Q., Xu, Z.: Development of a 10-year (2001–2010) 0.1° data set of land-surface energy balance for mainland China, Atmos. Chem. Phys., 14(23), 13097–13117, https://doi.org/10.5194/acp-14-13097-2014, 2014.

Chen, X., Su, Z., Ma, Y., Yang, K., Wen, J., Zhang, Y.: An Improvement of Roughness Height Parameterization of the Surface Energy Balance System (SEBS) over the Tibetan Plateau, J. Appl. Meteorol. Climatol., 52(3), 607–622, https://doi.org/10.1175/JAMC-D-12-056.1, 2013.

Chen, X., Su, Z., Ma, Y., Trigo, I., Gentine, P.: Remote Sensing of Global Daily Evapotranspiration based on a

Surface Energy Balance Method and Reanalysis Data, J. Geophys. Res. Atmos., 126(16), e2020JD032873, https://doi.org/10.1029/2020JD032873, 2021.

Chen, Y., Xia, J., Liang, S., Feng, J., Fisher, J. B., Li, X., Li, X., Liu, S., Ma, Z., Miyata, A., Mu, Q., Sun, L., Tang, J., Wang, K., Wen, J., Xue, Y., Yu, G., Zha, T., Zhang, L., Zhang, Q., Zhao, T., Zhao, L., Yuan, W.: Comparison of satellite-based evapotranspiration models over terrestrial ecosystems in China, Remote Sens. Environ., 140, 279–293, https://doi.org/10.1016/j.rse.2013.08.045, 2014.

Chen, Y., Yang, K., Tang, W., Qin, J., and Zhao, L.: Parameterizing soil organic carbon's impacts on soil porosity and thermal parameters for Eastern Tibet grasslands, Sci. China Earth Sci., 55(6), 1001–1011, https://doi.org/10.1007/s11430-012-4433-0, 2012.

Che, T., Li, X., Liu, S., Li, H., Xu, Z., Tan, J., Zhang, Y., Ren, Z., Xiao, L., Deng, J., Jin, R., Ma, M., Wang, J., and Yang, X.: Integrated hydrometeorological, snow and frozen-ground observations in the alpine region of the Heihe River Basin, China, Earth Syst. Sci. Data., 11, 1483–1499, https://doi.org/10.5194/essd-11-1483-2019, 2019.

Cleugh, H. A., Leuning, R., Mu, Q., Running, S. W.: Regional evaporation estimates from flux tower and MODIS satellite data, Remote Sens. Environ., 106(3), 285–304, https://doi.org/10.1016/j.rse.2006.07.007, 2007.

Cosby, B. J., Hornberger, G. M., Clapp, R. B., and Ginn, T. R.: A Statistical Exploration of the Relationships of Soil Moisture Characteristics to the Physical Properties of Soils, Water Resour. Res., 20(6), 682–690, https://doi.org/10.1029/WR020i006p00682, 1984.

Dan, J., Gao, Y., and Zhang, M.: tecting and Attributing Evapotranspiration Deviations Using Dynamical Downscaling and Convection-Permitting Modeling over the Tibetan Plateau, Water., 13(15), 2096: https://doi.org/10.3390/w13152096, 2017.

De Kok, R.J., Kraaijenbrink, P.D.A., Tuinenburg, O.A., Bonekamp, P.N.J., Immerzeel, W.W.: Towards understanding the pattern of glacier mass balances in High Mountain Asia using regional climatic modelling, Cryosphere, 14, 3215–3234, https://doi.org/10.5194/tc-14-3215-2020, 2020.

Denef, K., Galdo, I. D., Venturi, A., and Cotrufo, M. F.: Assessment of Soil C and N Stocks and Fractions across 11European Soils under Varying Land Uses, Open J. Soil Sci., 03(07), 297–313, https://doi.org/10.4236/ojss.2013.37035, 2013.

Dore, S., Montes-Helu, M., Hart, S. C., Hungate, B. A., Koch, G. W., Moon, J. B., Finkral, A., Kolb, T. E.: Recovery of ponderosa pine ecosystem carbon and water fluxes from thinning and stand-replacing fire,

Glob. Chang. Biol., 18(10), 3171–3185, https://doi.org/10.1111/j.1365-2486.2012.02775.x, 2012.

Ding, J., Chen, L., Ji, C., Hugelius, G., Li, Y., Liu, L., Qin, S., Zhang, B., Yang, G., Li, F., Fang, K., Chen, Y., Peng, Y., Zhao, X., He, H., Smith, P., Fang, J., Yang, Y.: Decadal soil carbon accumulation across Tibetan permafrost regions, Nature Geoscience, 10(6), 420–424, https://doi.org/10.1038/ngeo2945, 2017.

Eyring, V., Bony, S., Meehl, G. A., Senior, C. A., Stevens, B., Stouffer, R. J., Taylor, K. E.: Overview of the Coupled Model Intercomparison Project Phase 6 (CMIP6) experimental design and organization, Geosci. Model Dev., 9, 1937–1958. https://doi.org/10.5194/gmd-9-1937-2016, 2016.

Farouki, O.T.: The thermal properties of soils in cold regions, Cold Reg. Sci., Technol. 5, 67–75, https://doi.org/10.1016/0165-232X(81)90041-0, 1981.

Fischer, M. L., Billesbach, D. P., Berry, J. A., Riley, W. J., and Torn, M. S.: Spatiotemporal variations in growing season exchanges of CO2, H2O, and sensible heat in agricultural fields of the Southern Great Plains, Earth Interact., 11(17), https://doi.org/10.1175/EI231.1, 2007.

Camillo, P. J. and Gurney, R. J.: A resistance parameter for bare soil evaporation models, Soil Sci., 141(2), 95–105, https://doi.org/10.1097/00010694-198602000-00001, 1986.

Gan, R., Zhang, Y., Shi, H., Yang, Y., Eamus, D., Cheng, L., Chiew, F., Yu, Q.: Use of satellite leaf area index estimating evapotranspiration and gross assimilation for Australian ecosystems, Ecohydrology, 11(5), e1974, https://doi.org/10.1002/eco.1974, 2018.

Good, S. P., Noone, D., and Bowen, G.: Hydrologic connectivity constrains partitioning of global terrestrial water fluxes, Science, 349(6244), 175–177, https://doi.org/10.1126/science.aaa5931, 2015.

Han, C., Ma, Y., Chen, X., Su, Z.: Trends of land surface heat fluxes on the Tibetan Plateau from 2001 to 2012, Int. J. Climatol., 37, 4757–4767, https://doi.org/10.1002/joc.5119, 2017.

Han, C., Ma, Y., Wang, B., Zhong, L., Ma, W., Chen, X., and Su, Z.: Long term variations of actual evapotranspiration over the Tibetan Plateau, Earth Syst. Sci. Data., 13, 3513–3524, https://doi.org/10.5194/essd-13-3513-202, 2021.

He, J., Yang, K., Tang, W., Lu, H., Qin, J., Chen, Y., Li, X.: The first high-resolution meteorological forcing dataset for land process studies over China, Sci. Data., 7(1), 25, https://doi.org/10.1038/s41597-020-0369-y, 2020.

Immerzeel, W. W., Van Beek, L. P. H., Bierkens, M. F. P.: Climate change will affect the Asian water towers. Science, 2010, 328(5984), 1382–1385. https://doi.org/10.1126/science.1183188

Immerzeel, W. W., Lutz, A. F., Andrade, M., Bahl, A., Biemans, H., Bolch, T., Hyde, S., Brumby, S., Davies,

B., Elmore, A., Emmer, A., Feng, M., Fernández, A., Haritashya, U., Kargel, J., Koppes, M., Kraaijenbrink, P., Kulkarni, A., Mayewski, P., Nepal, S., Pacheco, P., Painter, T., Pellicciotti, F., Rajaram, H., Rupper, S., Sinisalo, A., Shrestha, A., Viviroli, D., Wada, Y., Xiao, C., Yao, T., Baillie, J. E. M.: Importance and vulnerability of the world's water towers, Nature, 577(7790), 364–369, https://doi.org/10.1038/s41586-019-1822-y, 2020.

Irmak, S., and Mutiibwa, D.: On the dynamics of canopy resistance: Generalized linear estimation and relationships with primary micrometeorological variables, Water Resour. Res., 46(8), W08526, https://doi.org/10.1029/2009WR008484, 2010.

Jarvis, P. G.: The InterprETtion of the Variations in Leaf Water Potential and Stomatal Conductance Found in Canopies in the Field. Philos, Trans. R. Soc. London. B, Biol. Sci., 273(927), 593–610, https://doi.org/10.1098/rstb.1976.0035, 1976.

Jiang, Y., Yang, K., Qi, Y., Zhou, X., He, J., Lu, H., Li, X., Chen, Y., Li, X., Zhou, B., Mamtimin, A., Shao, C., Ma, X., Tian, J., and Zhou, J.: TPHiPr: a long-term (1979–2020) high-accuracy precipitation dataset (1⁄30°, daily) for the Third Pole region based on high-resolution atmospheric modeling and dense observations, Earth Syst. Sci. Data, 15, 621–638, https://doi.org/10.5194/essd-15-621-2023, 2023.

Jung, M., Reichstein, M., Ciais, P., Seneviratne, S. I., Sheffield, J., Goulden, M. L., Bonan, G., Cescatti, A., Chen, J., De Jeu, R., Dolman, A., Eugster, W., Gerten, D., Gianelle, D., Gobron, N., Heinke, J., Kimball, J., Law, B., Montagnani, L., Mu, Q., Mueller, B., Oleson, K., Papale, D., Richardson, A., Roupsard, O., Running, S., Tomelleri, E., Viovy, N., Weber, U., Williams. C., Wood, E., Zaehle, S., Zhang, K.: Recent decline in the global land evapotranspiration trend due to limited moisture supply, Nature, 467(7318), 951–954, https://doi.org/10.1038/nature09396, 2010.

Khan, M. S., Liaqat, U. W., Baik, J., and Choi, M.: Stand-alone uncertainty characterization of GLEAM, GLDAS and MOD16 evapotranspiration products using an extended triple collocation approach, Agric. For. Meteorol., 252, 256–268, https://doi.org/10.1016/j.agrformet.2018.01.022, 2018.

Kuang, X., and Jiao, J. J.: Review on climate change on the Tibetan plateau during the last half century, J. Geophys. Res. Atmos., 121, 3979-4007, https://doi.org/10.1002/2015JD024728, 2016.

Kutsch, W. L., Aubinet, M., Buchmann, N., Smith, P., Osborne, B., Eugster, W., Wattenbach, M., Schrumpf, M., Schulze, E., Tomelleri, E., Ceschia, E., Bernhofer, C., Béziat, P., Carrara, A., Di Tommasi, P., Grunwald, T., Jones, M., Magliulo, V., Moureaux, C., Olioso, A., Sanz, M., Saunders, M., Søgaard, H.,

740   Ziegler, W.: The net biome production of full crop rotations in Europe, Agric. Ecosyst. Environ., 139(3), 336–345, https://doi.org/10.1016/j.agee.2010.07.016, 2010.

Kool, D., Agam, N., Lazarovitch, N., Heitman, J.L., Sauer, T.J., Ben-Gal, A.: A review of approaches for evapotranspiration partitioning, Agric. For. Meteorol., 184, 56–70, https://doi.org/10.1016/j.agrformet.2013.09.003, 2014.

745   Koster, R. D., and Suarez, M. J.: The Influence of Land Surface Moisture Retention on Precipitation Statistics. J. Clim., 9(10), 2551–2567, https://doi.org/10.1175/1520-0442(1996)009, 1996.

Lawrence, D. M., Thornton, P. E., Oleson, K. W., and Bonan, G. B.: The Partitioning of Evapotranspiration into Transpiration, Soil Evaporation, and Canopy Evaporation in a GCM: Impacts on Land–Atmosphere Interaction, J. Hydrometeorol., 8, 862–880, https://doi.org/10.1175/JHM596.1, 2007.

750   Lehmann, P., Merlin, O., Gentine, P., and Or, D.: Soil texture effects on surface resistance to bare soil evaporation, Geophys. Res. Lett., 45(19), 10, 398-10, 405, https://doi.org/10.1029/2018GL078803, 2018.

Lemone, M. A., Chen, F., Alfieri, J. G., Cuenca, R. H., Hagimoto, Y., Blanken, P., Niyogi, D., Kang, S., Davis, K., Grossman, R. L.: NCAR/CU surface, soil, and vegetation observations during the International H2O Project 2002 field campaign, Bull. Am. Meteorol. Soc, 88(1), 65–81, https://doi.org/10.1175/BAMS-88-1-65, 2007.

755   1-65, 2007.

Letts, M.G., Comer, N.T., Roulet, N.T., Skarupa, M.R., Verseghy, D.L.: Parametrization of peatland hydraulic properties for the Canadian land surface scheme, Atmos. Ocean., 38, 141–160, https://doi.org/10.1080/07055900.2000.9649643, 2000.

Leuning, R., Zhang, Y.Q., Rajaud, A., Cleugh, H., Tu, K.: A simple surface conductance model to estimate
760   regional evaporation using MODIS leaf area index and the Penman–Monteith equation, Water Resour., Res. 44 (10), W10419, https://doi.org/10.1029/2007WR006562, 2010.

Liang, S., Cheng, J., Jia, K., Jiang, B., Liu, Q., Xiao, Z., Yao, Y., Yuan, W., Zhang, X., Zhao, X., Zhou, J.: The global land surface satellite (GLASS) product suite, Bull. Am. Meteorol. Soc., 102, E323–E337, https://doi.org/10.1175/BAMS-D-18-0341.1, 2021.

765   Liu, J., Chai, L., Dong, J., Zheng, D., Wigneron, J. P., Liu, S., Zhou, J., Xu, T., Yang, S., Song, Y., Qu, Y., Lu, Z.: Uncertainty analysis of eleven multisource soil moisture products in the third pole environment based on the three-corned hat method, Remote Sens. Environ., 255, 112225, https://doi.org/10.1016/j.rse.2020.112225, 2021.

Liu, S., Lu, L., Mao, D., and Jia, L.: Evaluating parameterizations of aerodynamic resistance to heat transfer

770   using field measurements, Hydrol. Earth Syst. Sci., 11, 769–783, https://doi.org/10.5194/hess-11-769-2007, 2007.

Liu, S.M., Li, X., Xu, Z.W., Che, T., Xiao, Q., Ma, M.G., Liu, Q.H., Jin, R., Guo, J.W., Wang, L.X., Wang, W.Z., Qi, Y., Li, H.Y., Xu, T.R., Ran, Y.H., Hu, X.L., Shi, S.J., Zhu, Z.L., Tan, J.L., Zhang, Y., Ren, Z.G.: The Heihe Integrated Observatory Network: A Basin-Scale Land Surface Processes Observatory in China, 775   Vadose Zo. J., 17(1), 180072, https://doi.org/10.2136/vzj2018.04.0072, 2018.

Liu, S. M., Xu, Z. W., Wang, W. Z., Jia, Z. Z., Zhu, M. J., Bai, J., and Wang, J. M.: A comparison of eddy-covariance and large aperture scintillometer measurements with respect to the energy balance closure problem, Hydrol. Earth Syst. Sci., 15, 1291–1306, https://doi.org/10.5194/hess-15-1291-2011, 2011.

Li, S., Hao, X., Du, T., Tong, L., Zhang, J., Kang, S.: A coupled surface resistance model to estimate crop 780   evapotranspiration in arid region of northwest China, Hydrol. Process., 28(4), 2312–2323, https://doi.org/10.2136/vzj2018.04.0072, 2013.

Li, S., Wang, G., Sun, S., Chen, H., Bai, P., Zhou, S., Huang, Y., Wang, J., Deng, P.: Assessment of Multi-Source Evapotranspiration Products over China Using Eddy Covariance Observations, Remote Sens., 10(11), 1692, https://doi.org/10.3390/rs10111692, 2018.

785 Li, X., Liang, S., Yuan, W., Yu, G., Cheng, X., Chen, Y., Zhao, T., Feng, J., Ma, Z., Ma, M., Liu, S., Chen, J., Shao, C., Li, S., Zhang, X., Zhang, Z., Sun, G., Chen, S., Ohta, T., Varlagin, A., Miyata, A., Takagi, K., Saiqusa, N., Kato, T.: Estimation of evapotranspiration over the terrestrial ecosystems in China, Ecohydrology, 7(1), 139–149, https://doi.org/10.1002/eco.1341, 2014a.

Li, X., Wang, L., Chen, D., Yang, K., and Wang, A.: Seasonal evapotranspiration changes (1983-2006) of four 790   large basins on the Tibetan Plateau, J. Geophys. Res. Atmos., 119(23), 13,079–13,095, https://doi.org/10.1002/2014JD022380, 2014b.

Li, S., Zhang, L., Kang, S., Tong, L., Du, T., Hao, X., and Zhao, P.: Comparison of several surface resistance models for estimating crop evapotranspiration over the entire growing season in arid regions, Agric. For. Meteorol., 208, 1–15, https://doi.org/10.1016/j.agrformet.2015.04.002, 2015.

795 Long, D., Singh, V. P., and Li, Z.-L.: How sensitive is SEBAL to changes in input variables, domain size and satellite sensor?, J. Geophys. Res.-Atmos., 116, D21107, https://doi.org/10.1029/2011jd016542, 2011.

Ma, N., Szilagyi, J., Zhang, Y., Liu, W.: Complementary-Relationship-Based Modeling of Terrestrial Evapotranspiration Across China During 1982–2012: Validations and Spatiotemporal Analyses, J. Geophys. Res. Atmos., 124(8), 4326–4351, https://doi.org/10.1029/2018JD029850, 2019.

800   Ma, N., Zhang, Y.: Increasing Tibetan Plateau terrestrial evapotranspiration primarily driven by precipitation, Agric. For. Meteorol., 317, 108887, https://doi.org/10.1016/j.agrformet.2022.108887, 2022.

Ma, N., Zhang, Y., Guo, Y., Gao, H., Zhang, H., Wang, Y.: Environmental and biophysical controls on the evapotranspiration over the highest alpine steppe, J. Hydrol., 529, 980–992, https://doi.org/10.1016/j.jhydrol.2015.09.013, 2015.

805   Ma, N., Y. Zhang, C.-Y. Xu, and J. Szilagyi: Modeling actual evapotranspiration with routine meteorological variables in the data-scarce region of the Tibetan Plateau: Comparisons and implications, J. Geophys. Res. Biogeosci., 120, 1638–1657, https://doi.org/10.1002/2015JG003006, 2015.

Ma, Y., Hu, Z., Xie, Z., Ma, W., Wang, B., Chen, X., Li, M., Zhong, L., Sun, F., Gu, L., Han, C., Zhang, L., Liu, X., Ding, Z., Sun, G., Wang, S., Wang, Y., and Wang, Z.: A long-term (2005–2016) dataset of hourly
810   integrated land–atmosphere interaction observations on the Tibetan Plateau, Earth Syst. Sci. Data., 12, 2937–2957, https://doi.org/10.5194/essd-12-2937-2020, 2020.

Merlin, O., Stefan, V. G., Amazirh, A., Chanzy, A., Ceschia, E., Er-Raki, S., Khabba, S.: Modeling soil evaporation efficiency in a range of soil and atmospheric conditions using a meta-analysis approach, Water Resour. Res., 52(5), 3663–3684, https://doi.org/10.1002/2015WR018233, 2016.

815   Miralles, D. G., Holmes, T. R. H., De Jeu, R. A. M., Gash, J. H., Meesters, A. G. C. A., Dolman, A. J.: Global land-surface evaporation estimated from satellite-based observations, Hydrol. Earth Syst. Sci., 15(2), 453–469, https://doi.org/10.5194/hess-15-453-2011, 2011.

Miralles, D. G., Jiménez, C., Jung, M., Michel, D., Ershadi, A., McCabe, M. F., Hirschi, M., Martens, B., Dolman, A. J., Fisher, J. B., Mu, Q., Seneviratne, S. I., Wood, E. F., and Fernández-Prieto, D.: The
820   WACMOS-ET project – Part 2: Evaluation of global terrestrial evaporation data sets, Hydrol. Earth Syst. Sci., 20, 823–842, https://doi.org/10.5194/hess-20-823-2016, 2016.

Monteith, J.L.: Evaporation and environment. Symp. Soc. Exp. Biol., 19, 205–234, 1965.

Muñoz-Sabater, J., Dutra, E., Agustí-Panareda, A., Albergel, C., Arduini, G., Balsamo, G., Boussetta, S., Choulga, M., Harrigan, S., Hersbach, H., Martens, B., Miralles, D., Piles, M., Rodríguez-Fernández, N.,
825   Zsoter, E., Thépaut, J. N.: ERA5-Land: A state-of-the-art global reanalysis dataset for land applications, Earth Syst. Sci. Data, 13(9), 4349–4383, https://doi.org/10.5194/essd-13-4349-2021, 2021.

Mu, Q., Heinsch, F. A., Zhao, M., and Running, S. W.: Development of a global evapotranspiration algorithm based on MODIS and global meteorology data, Remote Sens. Environ., 111(4), 519–536. https://doi.org/10.1016/j.rse.2007.04.015, 2007.

830   Mu, Q., Zhao, M., and Running, S. W.: Improvements to a MODIS global terrestrial evapotranspiration algorithm, Remote Sens. Environ., 115(8), 1781–1800, https://doi.org/10.1016/j.rse.2011.02.019, 2011.

Novick, K. A., Stoy, P. C., Katul, G. G., Ellsworth, D. S., Siqueira, M. B. S., Juang, J., Oren, R.: Carbon dioxide and water vapor exchange in a warm temperate grassland, Oecologia., 138(2), 259–274, https://doi.org/10.1007/s00442-003-1388-z, 2004.

835   Ortega-Farias, S., Poblete-Echeverría, C., and Brisson, N.: Parameterization of a two-layer model for estimating vineyard evapotranspiration using meteorological measurements, Agric. For. Meteorol., 150(2), 276–286, https://doi.org/10.1016/j.agrformet.2009.11.012, 2010.

Peng, J., Loew, A., Chen, X., Ma, Y., and Su, Z.: Comparison of satellite-based evapotranspiration estimates over the Tibetan Plateau. Hydrol, Earth Syst. Sci., 20, 3167–3182, https://doi.org/10.5194/hess-20-3167-

840   2016, 2016.

Phillips, T. J., Klein, S. A., Ma, H. Y., Tang, Q., Xie, S., Williams, I. N., Joseph, A., David, R., Margaret, S.: Using ARM observations to evaluate climate model simulations of land-atmosphere coupling on the U.S. Southern Great Plains, J. Geophys. Res. Atmos., 122(21), 11,524–11, 548, https://doi.org/10.1002/2017JD027141, 2017.

845   Ramoelo, A., Majozi, N., Mathieu, R., Jovanovic, N., Nickless, A., and Dzikiti, S.: Validation of Global Evapotranspiration Product (MOD16) using Flux Tower Data in the African Savanna, South Africa, Remote Sens.-Basel, 6, 7406–7423, https://doi.org/10.3390/rs6087406, 2014.

Rodell, M., Houser, P. R., Jambor, U., Gottschalck, J., Mitchell, K., Meng, C. J., Arsenault, K., Cosgrovem B., Radakovich, J., Bosilovich, M., Entin, J., Walker, J., Lohmann, D., Toll, D.: The Global Land Data

850   Assimilation System, Bull. Am. Meteorol. Soc., 85, 381–394, https://doi.org/10.1175/BAMS-85-3-381, 2004.

Sakaguchi, K., Zeng, X.: Effects of soil wetness, plant litter, and under-canopy atmospheric stability on ground evaporation in the Community Land Model (CLM3.5), J. Geophys. Res., Atmos. 114(D1), https://doi.org/10.1029/2008JD010834, 2009.

855   Sellers, P. J., Randall, D. A., Collatz, G. J., Berry, J. A., Field, C. B., Dazlich, D. A., and Bounoua, L.: A Revised Land Surface Parameterization (SiB2) for Atmospheric GCMS. Part I: Model Formulation, J. Clim. 9(4), 676–705, https://doi.org/10.1175/1520-0442(1996)009<0676:ARLSPF>2.0.CO;2, 1996.

Schlesinger, W. H., and Jasechko, S.: Transpiration in the global water cycle, Agric. For. Meteorol., 189-190, 115–117, https://doi.org/10.1016/j.agrformet.2014.01.011, 2014.

860 Shi, Q., Liang, S.:Surface-sensible and latent heat fluxes over the Tibetan Plateau from ground measurements, reanalysis, and satellite data, Amos. Chem. Phys.,14, 5659–5677, https://doi.org/10.5194/acp-14-5659-2014, 2014.

Sobrino, J. A., Jiménez-Muñoz, J. C., and Paolini, L.: Land surface temperature retrieval from LANDSAT TM 5, Remote Sens. Environ., 90(4), 434–440, https://doi.org/10.1016/j.rse.2004.02.003, 2004.

865 Song, L., Zhuang, Q., Yin, Y., Zhu, X., and Wu, S.: Spatio-temporal dynamics of evapotranspiration on the Tibetan Plateau from 2000 to 2010, Environ. Res. Lett., 12(1), 014011, https://doi.org/10.1088/1748-9326/aa527d, 2017.

Su, Z.: The Surface Energy Balance System (SEBS) for estimation of turbulent heat fluxes, Hydrol. Earth Syst. Sci., 6, 85–100, https://doi.org/10.5194/hess-6-85-2002, 2002.

870 Sun, S.F.: Moisture and heat transport in a soil layer forced by atmospheric conditions, Master thesis, Dept. of Civil Engineering, University of Connecticut, 72, 1982.

Tang, J. Y. and Riley, W. J.: A new top boundary condition for modeling surface diffusive exchange of a generic volatile tracer: theoretical analysis and application to soil evaporation, Hydrol. Earth Syst. Sci., 17, 873–893, https://doi.org/10.5194/hess-17-873-2013, 2013.

875 Wang, B., Ma, Y., Su, Z., Wang, Y., and Ma, W.: Quantifying the evaporation amounts of 75 high-elevation large dimictic lakes on the Tibetan Plateau, Sci. Adv., 6(26), https://doi.org/10.1126/sciadv.aay8558, 2020.

Wang, G., Lin, S., Hu, Z., Lu, Y., Sun, X., and Huang, K.: Improving Actual Evapotranspiration Estimation Integrating Energy Consumption for Ice Phase Change Across the Tibetan Plateau, J. Geophys. Res. Atmos., 125(3), e2019JD031799, https://doi.org/10.1029/2019JD031799, 2020.

880 Wang, W., Li, J., Yu, Z., Ding, Y., Xing, W., Lu, W.: Satellite retrieval of actual evapotranspiration in the Tibetan Plateau: components partitioning, multi decadal trends and dominated factors identifying, J. Hydrol., 559, 471–485, https://doi.org/10.1016/j.jhydrol.2018.02.065, 2018.

Wang, Y., Lv, W., Xue, K. et al. Grassland changes and adaptive management on the Qinghai–Tibetan Plateau. Nat. Rev. Earth. Environ 3, 668–683 (2022). https://doi.org/10.1038/s43017-022-00330-8

885 Wei, Z., Yoshimura, K., Wang, L., Miralles, D. G., Jasechko, S., Lee, X.: Revisiting the contribution of transpiration to global terrestrial evapotranspiration. Geophysical Research Letters, 44, 2792–2801. https://doi.org/10.1002/2016GL072235

Wieder, W.R., J. Boehnert, G.B. Bonan, and M. Langseth.: Regridded Harmonized World Soil Database v1.2. Data set, Available on-line [http://daac.ornl.gov] from Oak Ridge National Laboratory Distributed Active

890   Archive Center, Oak Ridge, Tennessee, USA, http://dx.doi.org/10.3334/ORNLDAAC/1247, 2014.

Wilcox, B.P., Breshears, D.D., Seyfried, M.S.: Water balance on rangelands, In: Stewart, B.A., Howell, T.A. (Eds.), Encyclopedia of Water Science, Marcel Dekker Inc, New York, 791–794, http://www.cprl.ars.usda.gov/wmru/pdfs/DekkerEvettTDR.pdf, 2003.

Wu, C., Hu, B. X., Huang, G., and Zhang, H.: Effects of climate and terrestrial storage on temporal variability

895   of actual evapotranspiration, J. Hydrol., 549, 388–403, https://doi.org/10.1016/j.jhydrol.2017.04.012, 2017.

Yang, K., He, J., Tang, W., Qin, J., Cheng, C. C. K.: On downward shortwave and longwave radiations over high altitude regions: Observation and modeling in the Tibetan Plateau, Agric. For. Meteorol., 150(1), 38–46, https://doi.org/10.1016/j.agrformet.2009.08.004, 2010.

Yang, K., Koike, T., Ishikawa, H., Kim, J., Li, X., Liu, H., Liu S., Ma Y., Wang, J.: Turbulent flux transfer over

900   bare-soil surfaces: Characteristics and parameterization, J. Appl. Meteorol. Climatol., 47(1), 276–290, https://doi.org/10.1175/2007JAMC1547.1, 2008.

Yang, K., Wu, H., Qin, J., Lin, C., Tang, W., and Chen, Y.: Recent climate changes over the Tibetan Plateau and their impacts on energy and water cycle: A review, Glob. Planet. Change., 112, 79–91, https://doi.org/10.1016/j.gloplacha.2013.12.001, 2014.

905 Yang, Y., Liu, Y., Li, M., Hu, Z., Ding, Z.: Assessment of reanalysis flux products based on eddy covariance observations over the Tibetan Plateau, Theor. Appl. Climatol., 138, 275–292, https://doi.org/10.1007/s00704-019-02811-1, 2019.

Yao, T., Thompson, L., Yang, W., Yu, W., Gao, Y., Guo, X., Yang, X., Duan, K., Zhao, H., Xu, B., Pu, J., Lu, A., Xiang, Y., Kattel, D., Joswiak, D.: Different glacier status with atmospheric circulations in Tibetan

910   Plateau and surroundings, Nature Clim.Change, 2(9), 663–667, https://doi.org/10.1038/nclimate1580, 2012.

Yao, Y., Liang, S., Cheng, J., Liu, S., Fisher, J. B., Zhang, X., Jia, K., Zhao, X., Qin, Q., Zhao, B., Han, S., Zhou, G., Li, Y., Zhao, S.: MODIS-driven estimation of terrestrial latent heat flux in China based on a modified Priestley-Taylor algorithm, Agric. For. Meteorol., 171–172, 187–202,

915   https://doi.org/10.1016/j.agrformet.2012.11.016, 2013.

Yin, Y., Wu, S., Zhao, D., Zheng, D., Pan, T.: Modeled effects of climate change on actual evapotranspiration in different eco-geographical regions in the Tibetan Plateau, J. Geogr. Sci., 23(2), 195–207, https://doi.org/10.1002/eco.1341, 2013.

You, Q., Xue, X., Peng, F., Dong, S., Gao, Y.: Surface water and heat exchange comparison between alpine

920   meadow and bare land in a permafrost region of the Tibetan Plateau, Agric. For. Meteorol., 232, 48–65, https://doi.org/10.1016/j.agrformet.2016.08.004, 2017.

Yuan, L., Ma, Y., Chen, X., Wang, Y., Li, Z.: An enhanced MOD16 evapotranspiration model for the Tibetan Plateau during the unfrozen season, J. Geophys. Res. Atmos., 126, e2020JD032787, https://doi.org/10.1029/2020JD032787, 2021.

925   Yu, G. R., Wen, X. F., Sun, X. M., Tanner, B. D., Lee, X., Chen, J. Y.: Overview of ChinaFLUX and evaluation of its eddy covariance measurement, Agric. For. Meteorol., 137(3–4), 125–137, https://doi.org/10.1016/j.agrformet.2006.02.011, 2006.

Zhang, G., T. Yao, H. Xie, K. Yang, L. Zhu, C. K. Shum, T. Bolch, S. Yi, S. Allen, L. Jiang, W. Chen, and C. Ke: Response of Tibetan Plateau lakes to climate change: Trends, patterns, and mechanisms, Earth-Science

930   Reviews, 103269. https://doi.org/10.1016/j.earscirev.2020.103269, 2020.

Zhang, L. M., Luo, Y. W., Liu, M., Chen, Z., Su, W., He et al.: Carbon and water fluxes observed by the Chinese Flux Observation and Research Network (2003–2005) (in Chinese), Sci. Data., 4(1), https://doi.org/10.11922/csdata.2018.0028.zh, 2019.

Zhang, K., Kimball, J. S., Nemani, R. R., and Running, S. W.: A continuous satellite-derived global record of

935   land surface evapotranspiration from 1983 to 2006, Water Resour. Res., 46(9), W09522, https://doi.org/10.1029/2009WR008800, 2010.

Zhang, Y., Kong, D., Gan, R., Chiew, F. H. S., McVicar, T. R., Zhang, Q., and Yang, Y.: Coupled estimation of 500 m and 8-day resolution global evapotranspiration and gross primary production in 2002–2017, Remote Sens. 820 Environ., 222, 165–182, https://doi.org/10.1016/j.rse.2018.12.031, 2019b.

940   Zhang, Y., Peña-Arancibia, J. L., McVicar, T. R., Chiew, F. H. S., Vaze, J., Liu, C., Lu, X., Zheng, H., Wang, Y., Liu, Y., Miralles, D., Pan, M.: Multi-decadal trends in global terrestrial evapotranspiration and its components, Sci. Rep., 6, 19124, https://doi.org/10.1038/srep19124, 2016.

Zhao, H., Zeng, Y., Lv, S., and Su, Z.: Analysis of soil hydraulic and thermal properties for land surface modeling over the Tibetan Plateau, Earth Syst. Sci. Data., 10, 1031–1061, https://doi.org/10.5194/essd-10-

945   1031-2018, 2018.

Zheng, D., Zhang, Q., Wu, S.: Mountain genecology and sustainable development of the Tibetan Plateau, Springer Science & Business Media, 57, 2000.

Zhong, L., Ma, Y., Hu, Z., Fu, Y., Hu, Y., Wang, X., Cheng, M., and Ge, N.: Estimation of hourly land surface heat fluxes over the Tibetan Plateau by the combined use of geostationary and polar-orbiting satellites,

950   Atmos. Chem. Phys., 19, 5529–5541, https://doi.org/10.5194/acp-19-5529-2019, 2019.

Zohaib, M., H. Kim, and M. Choi.: Evaluating the patterns of spatiotemporal trends of root zone soil moisture in major climate regions in East Asia, J. Geophys. Res. Atmos., 122, 7705–7722, https://doi.org/10.1002/2016JD026379, 2017.